

NASA Contractor Report 174680

MEASUREMENT OF LOCAL CONNECTIVE HEAT TRANSFER COEFFICIENTS OF FOUR ICE  
ACCRETION SHAPES

Mark E. Smith, Rao V. Arimilli, and Edward G. Keshock

The University of Tennessee

Knoxville, Tennessee 37996-2210

May 1984

Prepared for

NATIONAL AERONAUTICS AND SPACE ADMINISTRATION  
Lewis Research Center  
Under Grant NAG-3-83

## TABLE OF CONTENTS

CHAPTER	PAGE
I. Introduction .....	1
II. The Experimental Method .....	3
Review of Experimental Methods .....	3
Selection of the Method for the Present Study .....	9
Heating Box .....	10
Wind Tunnel .....	11
Models .....	12
Data Acquisition .....	13
Test Procedure .....	13
Data Reduction .....	14
III. Test Results .....	17
Data Code .....	17
Circular Cylinder .....	17
15-Minute Rime Ice Shape .....	20
2-Minute Glaze Ice Shape .....	22
5-Minute Glaze Ice Shape .....	23
15-Minute Glaze Ice Shape .....	24
IV. Conclusions .....	27
List of References .....	29
Appendix A .....	60
Appendix B .....	63
Appendix C .....	69
Appendix D .....	71

<b>CHAPTER</b>	<b>PAGE</b>
<b>Appendix E .....</b>	<b>73</b>
<b>Appendix F .....</b>	<b>83</b>
<b>Appendix G .....</b>	<b>85</b>
<b>Appendix H .....</b>	<b>93</b>

## CHAPTER I

### INTRODUCTION

The experimental investigation of the ice accretion process is of prime interest in aircraft design. Components that have been under investigation include inlets, wings and rotors. The flight safety of an aircraft flown into icing conditions may be affected in a very short time. For example Lake and Bradley [1] have documented a case in which intolerable rotor icing conditions on a helicopter were reached within minutes of the onset of icing.

The deleterious effects of ice accretion on airfoil characteristics are well known. When ice forms at the leading edge of an airfoil during flight conditions its effect on the performance is devastating [2]. The airfoil suffers a loss in maximum lift and an increase in drag.

Ice accretion on airfoil surfaces is a result of flight into a region of super cooled water droplets. The two principal formations of accreted ice are rime ice and glaze ice. Rime ice occurs when the water droplets are highly super cooled and freeze immediately on contact with the surface. Glaze ice occurs when the liquid water content of the atmosphere is high and the droplets are not so highly super cooled. Water droplets impinge on the surface, a fraction of which runs back along the wing surface before freezing. Reference [3] gives a more thorough description of the conditions necessary for the formation of ice accretions.

A significant parameter in the analysis of the ice accretion process is the local convective heat transfer coefficient. It is easily seen that the accretion of glaze ice is dependent on the rate of heat transfer out of the dynamic freezing zone (the zone where the solidification of the impinging droplets occurs). The

extent of runback and thus the shape of the ice accretion is dependent on the rate of solidification, which in turn is dependent on the rate at which the heat of fusion may be released to the surroundings. What may not be so obvious is that the formation of rime ice is also dependent on the heat transfer out of the dynamic freezing zone. Immediate freezing of the impinging water droplets is said to occur as long as the Ludlam limit (defined as the maximum liquid water content of the free stream corresponding to the case where all impinging drops are frozen on impact) is not exceeded. To check for this it is necessary to consider the heat transfer processes within the dynamic freezing zone and its surroundings and thus the convective heat transfer coefficient is a required parameter.

In past studies various methods have been used to predict the local convective heat transfer coefficients. Commonly, the coefficient used is a derivative of the study of flow about a circular cylinder. For example, Lowzowski, et. al.[4] have used local Nusselt numbers for smooth and rough circular cylinders as suggested by Achenbach [5]. They acknowledge a need for quantitative data for local heat transfer on icing cylinders. Ackley and Templeton have used an average heat transfer coefficient taken from Bosch's formula [6].

The purpose of this experimental study was to provide more accurate information on the convective heat transfer characteristics of ice shapes than what was currently being used (i.e. ice shapes vs. circular cylinders). The objectives were to select a method of determining local convective heat transfer coefficients and, using that method, to evaluate the four ice accretion shapes shown in Figure 1. The shapes represented three stages of glaze ice formation and one rime ice formation. To simulate the roughness of the ice it was desired that the ice shapes be tested with rough surfaces. The test program employed a graded approach in which the ice shapes had initially smooth surfaces. The shapes then had increasing degrees of roughness applied to them.

## CHAPTER II

### THE EXPERIMENTAL METHOD

#### Review Of Experimental Methods

A number of experimental methods for determining local convective heat transfer coefficients were examined for possible use in this study. A review of these methods follows:

1. Thin-Skin Heat-Rate Measurement (Ref. 7)

The thin-skin technique is accepted as one of the accurate methods of convective heat transfer measurement. It is a transient method in which the model is either heated or cooled by the air stream while the skin temperatures are recorded with time. The thin-skin temperature data are reduced to coefficient form using the calorimetric heat balance as follows.

$$h = \frac{\rho bc}{T_r - T} \frac{dT}{dt} \quad (1)$$

where the symbols are defined as:

- b = model skin thickness
- c = model skin material specific heat
- h = heat transfer coefficient
- t = time
- T = skin temperature
- T<sub>r</sub> = free stream temperature
- ρ = model skin material density

The above equation is based on the assumption that all heat transfer is due to convection. Radiation and conduction effects are assumed to be negligible. This assumption is valid with regard to radiation since radiation effects in wind tunnels are small. However, conduction effects due to temperature gradients along the skin frequently appear and lead to considerable uncertainty in data. Methods to predict conduction effects have been developed for special cases but their general application is at best difficult.

A technique using equation (1) in a different form has been developed to avoid problems with conduction effects. The equation is integrated to put it in the form

$$\frac{h}{\rho b c} (t - t_i) = \ln \left[ \frac{T_r - T_i}{T_r - T} \right] \quad (2)$$

If equation (2) is then differentiated to put it in the form

$$h = \rho b c \frac{d}{dt} \ln \left[ \frac{T_r - T_i}{T_r - T} \right] \quad (3)$$

since  $h$ ,  $\rho$ ,  $b$ , and  $c$  are constants it can be seen that the term

$$\ln \left[ \frac{T_r - T_i}{T_r - T} \right]$$

must be linear with time if the original assumptions are not violated. If the log term is not linear with time then the assumptions have been violated.

This knowledge gives rise to a data reduction procedure in which the log term is plotted against time and the plots are examined for non-linearities. The rate of change of the slope (the non-linearity) is a direct indication of the errors present in the data. Data is then chosen to avoid the non-linearity thus avoiding the errors.

Using this approach, then, the data must be plotted in terms of log vs. time and evaluated to determine which thermocouples are subject to conduction errors.

## 2. Discrete Point Methods (Ref. 7)

This section covers a number of methods similar to the thin-skin method, the difference being that the heat rate is measured at isolated points. Typical of these methods is the use of the Gardon gage, shown in Figures 2 and 3. There are two copper-constantan thermocouple junctions in this arrangement, one at the center of the disc and one at the edge of the disc. The equation relating the incident heat flux to the temperature difference across the disc is

$$q = \frac{4kb}{R^2} (T_c - T_e) \quad (4)$$

where the symbols are defined in Figure 2.

Note that the heat flux is directly proportional to the temperature difference. Thus the output of the gage, (which is a result of the temperature difference) is also directly proportional to the incident heat flux.

It is possible to insulate the Gardon gage to reduce or eliminate conduction effects. Also the dimensions required for calculating the heat flux ( $R$ ,  $b$ ) may be accurately known and are in fact given in a calibration factor, along with other constant factors, so that the heat flux may be calculated directly from the electrical output.

The difficulty with using the discrete point techniques is in the preparation of the model. The temperature sensing devices (e.g, the Gardon gage) must be installed so that they are exposed to the convective air stream, but the model surface must be smooth. In the case of the Gardon gage there will be a



discontinuity of the model surface at the gage because the gage surface cannot be formed to accomodate the curve of the model surface.

A device that avoids this problem is the coaxial thermocouple gage (Figure 4). It consists of an insulated Chromel wire fixed concentrically within a constantan jacket. The thermocouple is mounted on the model so that it protrudes above the surface of the model. The thermocouple is then filed down so that it conforms exactly to the surface of the model. In the process of filing the thermocouple materials are blended together to form the thermocouple junction.

Data reduction is accomplished by modeling the coaxial gage as a one-dimensional, semi-infinite solid. With this model the gage output is directly proportional to the square root of the run time for a step input of constant heat flux at the surface.

### 3. Phase Change Paint Method (Ref. 7)

The phase change paint technique makes use of a paint that melts at a specific temperature. The paint changes from an opaque solid to a transparent liquid when it melts thus giving an accurate visual indication of the surface temperature. The painted model is injected into the wind tunnel. High speed cameras record the time response of the paint as it melts. The heat flux can then be determined from the time response of T using the equation

$$h = \frac{\beta \sqrt{\rho c k}}{\sqrt{t}} \quad (5)$$

where  $\beta$  is determined using the equation

$$\frac{T - T_i}{T_r - T_i} = 1 - e^{\beta^2} \operatorname{erfc}(\beta) \quad (6)$$

- $\rho$  = model material density
- $c$  = model material specific heat
- $k$  = model material thermal conductivity
- $T_i$  = model initial temperature
- $T_r$  = free stream recovery temperature

One of the advantages of using this method is that complex model shapes can be used. The main disadvantage of this method is the difficulty in obtaining quantitative data. Because of the difficulties in determining the properties in the parameter  $\sqrt{\rho ck}$ , its value can rarely be known better than within 10 percent. Thus the precision of the heat transfer coefficient is about 15 percent when all error contributions are considered.

#### 4. Liquid Crystal Method

The use of liquid crystals to determine convective heat transfer is described by Hippensteele, et al. [8]. The model surface to be investigated is covered by a composite skin consisting of an outer layer of liquid crystal sheet and an inner layer of a heating element sheet. The composite sheet is calibrated for heating uniformity. Then the sheet is applied to the model and calibrated in this configuration to obtain heat losses. The heat transfer is calculated using the equation

$$q_e - q_l = h A (T_c - T_a) \quad (7)$$

where

- $q_e$  = electric power applied (corrected using the calibration)
- $q_l$  = heat transfer losses
- $T_c$  = model surface temperature determined by observation of the liquid crystal's color
- $T_a$  = ambient air temperature

One of the problems with this method is that although it can be very accurate, it requires subjective judgment to determine the color and thus the temperature of the surface. This disadvantage can be minimized if the person that is making the judgment is "calibrated" using a portion of the liquid crystal sheet in a controlled temperature water bath.

Another limitation of the method is that the liquid crystal/heating element composite cannot take compound curves. Thus the geometry of the model must be simple. This limitation could be overcome with the use of liquid crystals in slurry form and conductive paint for a heating element. The technique would, however, require development.

#### 5. Napthalene Sublimation Method

Measurement of the sublimation rate of solid napthalene is a well proven method for determining mass-transfer coefficients in convective situations [9]. Because the heat and mass transfer equations are analogous, the technique can be used to predict heat transfer coefficients. The problem of measuring heat transfer rate is thus converted to the problem of measuring mass transfer rate. Average mass transfer rates can be determined by use of a weighing technique. Local mass transfer rates can be measured by several methods. A conceptually simple method is that of spraying the surface in question with a thin napthalene film of controlled thickness. The surface is then subjected to convective conditions and the time for the napthalene film to clear locally is observed. In another similar technique the napthalene does not clear the surface. Rather, accurate physical measurements are made before and after convection to determine the amount of sublimed napthalene.

It can be seen that the use of napthalene sublimation requires very accurate experimental procedures. In the technique where the napthalene is allowed to

clear from the surface, the initial film must be applied in an accurately controlled thickness. A technique for doing this on complex surfaces is not known. In the technique where the naphthalene surface is measured, it is essential that the measurements be accurate. It is difficult to achieve the required accuracy by mechanical measurements. A measurement technique which utilizes laser holographic interferometry has been investigated but has been fruitless [10]. In both of these techniques the temperature of the convective stream must be held constant. The sublimation rate changes by 10% with a temperature change of 1 °C.

#### Selection Of the Method For the Present Study

The thin-skin method was chosen based on the criteria that the method be simple and usable with the low-speed wind-tunnel at the University of Tennessee. Naphthalene sublimation was not pursued because the measurements required to determine the amount of sublimed naphthalene would be extremely difficult with some of the more complex model shapes. The use of phase change paint was not considered because it would require extensive modification of the wind-tunnel. Use of the liquid crystal method was not initially ruled out, but the testing technique would have to be developed before the method could be used. The thin-skin method was chosen over the discrete point methods for its simplicity.

Normal practice with the thin-skin method is to inject the model to be tested into the wind-tunnel air stream. The initial skin temperature of the model is different from the air stream temperature. The transient skin temperatures are recorded with time and the heat transfer calculated from that data.

It was necessary to design an apparatus for injection of a model into the wind-tunnel at UT. A method was considered in which the model is fixed in the wind-tunnel and heated in place by radiation from theater type lights. Rough

calculations showed that an unreasonable amount of power would be required to reach the desired initial temperature. Also, as it was learned later while testing, radiant heating would produce a very non-uniform temperature distribution on the model skin which would result in unreliable data.

The decision was made to build a device that would heat the model before injection into the tunnel. This "heating box" is shown in Figure 5 and is described in the next section. It consisted of an oven-like box equipped with a mechanism that would inject the model into the wind-tunnel while the wind-tunnel was running. With this device it was possible to perform a thin-skin heat rate measurement in a manner similar to that employed conventionally in the aerospace industry.

### Heating Box

The heating box was the device for heating the model and injecting it into the wind-tunnel (Figure 5). The mechanism for injecting the model was a long swinging arm on which the model was mounted. The model could be positioned inside the box for heating or outside the box in the run position. There was an opening in the face of the box through which the model entered the wind-tunnel. When the model was in the heating position this opening was closed off by a door. At the initiation of injection the door opened into the wind-tunnel. While the model was in the wind-tunnel the door lay against the face of the heating box downstream of the model.

Two schemes were used for model heating. The first was the use of infrared radiation from quartz tubes mounted on a reflector. The resulting temperature distribution around the circumference of the model was not uniform using this

scheme of heating which led to uncertainty about test results (see Appendix A for more details). In the configuration used for experimentation the air inside the box was heated by two finned heating elements. A fan was used to circulate air through the heating elements thus creating a more uniform temperature. The temperature distribution could then be held to within a 1.5 ° F difference over a 0.25 inch span if the need arose.

The heating box had some other important features. One entire side of the box was removable for access to its interior. All of the moving parts could be disassembled and removed from the box for modification or replacement. The box was supported on a wheeled stand and could be removed from the wind-tunnel by releasing two clamps. This allowed easy conversion back to normal wind-tunnel use.

### Wind Tunnel

The wind tunnel was an open circuit, closed test section type with the fan downstream of the test section. The tunnel had a speed range of 0-200 mph. The turbulence level was 0.5% or less. The speed measurement was made by a calibrated manometer that showed the difference between the test section static pressure and the external ambient pressure.

The test section was 28 inches by 20 inches in cross-section. It was accessible from either side through plexiglass doors hinged at the top. In the configuration used for this test one of the doors was removed. The face of the heating box took the place of that door and became a wall of the test section.

## Models

The models consisted of a wooden substructure to which metal skins were attached (Figure 6). The models had a span of 12 inches and represented ice accretion on a cylinder of 2.5 inches diameter. The shapes for the ice accretions were provided by NASA. They were obtained by accreting ice on a 2 inch diameter cylinder in the icing wind tunnel. It was not possible to form the skin exactly to the shape desired (maximum error was approximately  $\pm 0.25$  inches). The coordinates of the shapes as they were tested are given in Tables 1 through 4 along with the Figures 9, 14, 17, 20, and 23. The models were supported in the center of the test section by an 8 inch long, 2 inch diameter tube.

The wooden substructure was designed so that the metal skin would have a minimum of contact with the wood itself. The skin was attached to it by a row of screws running spanwise along each of its edges. There was an air space behind the skin that insulated the skin from the wood substructure. This air space was sealed to prevent convective currents on the back of the skin. The air space was 0.25 inch thick when the skin for modeling a cylinder was used. The thickness of the air space, of course, varied with other skin shapes.

The skin was 0.015 inch thick stainless steel. The thermocouples were attached to the back of the skin using a capacitive discharge welder. The thermocouple wires were anchored to the skin about 0.5 inch from the thermocouple junctions by spot-welding a stainless steel shim stock strap across them. This followed the method suggested in Reference 11. To eliminate effects of the finite aspect ratio, the thermocouples were located at midspan. The thermocouple wire was 30 gauge copper-constantan with glass braid sheaths. The properties of the skin material, density and specific heat, were determined by normal methods.

### Data Acquisition

A Hewlett Packard model 9826 microcomputer was used in conjunction with a Hewlett Packard model 3497A analog/digital scanning voltmeter to record times and temperatures during testing. The scanning voltmeter serially scanned the thermocouples and stored the voltage data. The computer's internal clock provided the timebase. The program used for data acquisition and reduction is provided in Appendix B.

The air temperature inside the heating box was monitored with an Omega model 2166A digital thermometer.

### Test Procedure

In preparation to test, the computer was turned on and the reference thermocouple was put in an ice bath. The model was put in the run position (in the wind-tunnel) while the heating box came up to temperature.

When the interior temperature of the box had stabilized at a temperature between 340°F and 380°F the model was pulled into the box, the door of the box was closed, and the model was allowed to heat up. The thermocouples on the model were monitored, and when the temperatures reached about 300°F the wind-tunnel was started and the desired air speed was set. The data acquisition was started and approximately 1 second later, the model was injected into the tunnel. While data were being recorded, the air speed in the tunnel was also recorded. (The air speed would be different than what was set before the model was injected.)



If more tests were to be conducted the model was allowed to continue cooling in the air stream to protect the wooden model substructure from excessive temperatures. After sufficient cooling the wind-tunnel was stopped and the test procedure was repeated.

### Data Reduction

The computer program for storing digitized data also computed the heat transfer coefficient and for the ice shapes the film temperature and Nusslet number were calculated as well. Appendix C contains more information. The computation was done for each reading of a thermocouple using the previous reading of the same thermocouple as the initial reading, and by assuming a linear relationship between  $\ln [(T_r - T_i)/(T_r - T)]$  and time between successive readings of each thermocouple. Thus, equation (2) was used in the form

$$h = \rho bc \frac{\ln \left[ \frac{T_r - T_i}{T_r - T} \right]}{(t - t_i)} \quad (7)$$

Part of the difficulty with using the thin-skin method was the elimination of conduction errors. Although a plot of  $\ln [(T_r - T_i)/(T_r - T)]$  against time would be linear unless conduction errors were present, the non-linearity was small in magnitude and was difficult to detect. The possibility of conduction errors arose mainly because some regions of the model's surface cooled more rapidly than others which created circumferential temperature gradients. The end result was that the Nusselt numbers calculated during data reduction varied with time as the degree of conduction along the skin varied.

As mentioned previously, Trimmer et al.[7] suggested that conduction errors could be avoided if the data used was such that

$$\ln \left[ \frac{T_r - T_i}{T_r - T} \right]$$

was linear with time. For the conditions of this study the non-linearities were not obvious even when severe conduction errors were expected.

By plotting some of the data on a greatly expanded scale it was determined that conduction errors could be avoided by using data sufficiently close to the time of injection while still avoiding the injection transient. A good example of this is the 15 minute rime ice shape where severe temperature gradients were established soon after injection. Data is plotted on a greatly expanded scale shown in Figure 7 where it can be seen that after the second scan following injection the data became non-linear. Thus the first and second scans after injection were used for data reduction.

Another indication of the best data to use was gained by observing the change of Nusselt number with time in areas of high heat transfer. For areas where there was a sharp heat transfer peak, the Nusselt number would rise until conduction caused it to decrease. Figure 8 shows the change in Nusselt number with time. The injection occurred during the first scan shown. The Nusselt number reached a maximum at thermocouple 4 during the second scan after injection. As time continued the temperature gradients had the effect of smoothing out the Nusselt number curve.

To pick the best data a combination of indicators were used. Primarily, data near the injection were used. If the model had a sharp peak in heat transfer, a peak in Nusselt number with time was used as an indicator. Using these criteria it turned out that the data used was from either the first and second scans or the second and third scans for each model.

For all models used in this study the Nusselt number and Reynolds number were calculated using the film temperature and a characteristic length of 2.5 inches (the diameter of the wooden cylinder on which the thin-skin is mounted). The film temperature was calculated by averaging the skin temperatures, then averaging that temperature with the free stream temperature.

$$Re_d = \frac{Ud}{\nu} \quad (8)$$

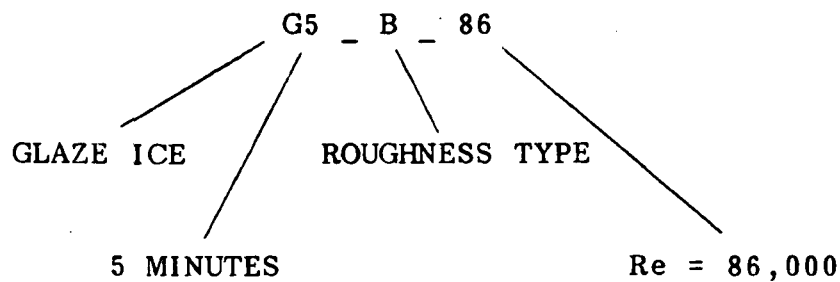
$$Nu = \frac{hd}{k} \quad (9)$$

## CHAPTER III

### TEST RESULTS

#### Data Code

To ease handling and identification of the data each set of data was assigned a data code. An example of the data code is given below.



The first letter indicates a rime or glaze ice shape. The following number indicates the number of minutes of ice accumulation that produced that shape. The letters after the first underbar indicate the surface condition. They are SM for smooth, SP for a sandpaper strip, B for roughness "B", and D for roughness "D". The number after the second underbar are the thousands digits of the Reynolds number at which the test was conducted.

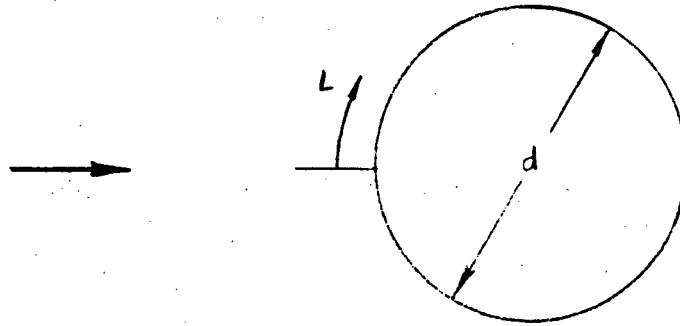
#### Circular Cylinder

Initial tests were run on a circular cylinder model so that the experimental method could be proven against available information. An analytical equation

developed by Frossling [12] was used as a basis for evaluating the experimental results. The equation is

$$\frac{Nu}{\sqrt{Re_d}} = 0.9449 - 0.51 X^2 - 0.5956 X^4 \quad (10)$$

where  $X = L/d$



The equation is for a laminar boundary layer and does not account for transition to a turbulent boundary layer or for separation of the boundary layer.

Some problems were encountered in the initial tests which may be of interest to other experimenters considering the use of the thin-skin heat rate technique. A discussion of these problems and their solutions is included in Appendix D.

The circular cylinder with the thermocouple locations is shown in Figure 9. The results are given in Figure 10 and in Table 4 in Appendix E. The results agreed with equation (10) within approximately  $\pm 15\%$ . The uncertainty analysis is presented in Appendix F. The uncertainty is highly sensitive to the rate of temperature change. For this reason the maximum uncertainties, in units of  $Nu$ , are given in the figures where the results are presented. Uncertainty bands for the maximum  $Re$  cases are also given in the figures where the smooth surface results appear.

To simulate a rough surface, stainless steel wires were attached to the model as shown in Figure 11. The wires were 0.020 inch in diameter and ran span-wise on the model. The wires were situated between the thermocouples so that the thermal mass of the skin at the thermocouples would not be affected. For the cylinder the wires were held to the surface by wires wrapped around the cylinder approximately 1 inch away for the thermocouples. For the ice shapes the wires were attached to the surface using the thermocouple welder. This configuration was called roughness "B" and the results appear in Figure 12 and in Table 6 in Appendix E.

Roughness "B" greatly enhanced the heat transfer of the circular cylinder. The curves of Figure 12 are qualitatively similar to the findings of Achenbach [5] for rough surfaced cylinders. Achenbach's results and the results of the present study cannot be compared quantitatively because the roughness heights and Reynolds numbers used in the two studies are not comparable.

Actual ice accretions can be very rough. Therefore a method of further roughening the surface, designated as roughness "D" was tried. Roughness "D", shown in Figure 13, consisted of 0.020 inch stainless steel wires which had loops spaced at approximately 0.25 inch intervals. The loops were made by twisting the wire one turn giving a loop height of approximately 0.125 inches. The actual height of the loops above the model surface was difficult to determine since the wires could not always be made to lie on the model's surface. The wires were attached to the models in the same way as for roughness "B". The loops spanned approximately 5 inches at the center of the model and ran span-wise between thermocouples.

The results of the circular cylinder with roughness "D" are shown in Figure 12 and Table 7 in Appendix E. It is interesting to note that the maximum Nusselt

numbers were less for roughness "D" than for roughness "B". It was speculated that this was caused by a thickening of the boundary layer due to the projections (the loops). As mentioned previously, the thermocouples were in the "valleys" between the trip wires on the model surface. The average heat transfer in these "valleys" would be expected to be less than an average heat transfer for the fully rough surface.

#### 15-Minute Rime Ice Shape

The shape for 15 minutes of rime ice accumulation, shown in Figure 14 with coordinates given in Table 1, was tested extensively and was used to further validate the method by comparison to results of NASA in-house tests[13]. There was some apprehension when the results of this study did not agree with the NASA results. An investigation of the differences between the two studies was conducted and it was concluded that the disagreements were due to differences in the models and the flow conditions and with identical test conditions the results would be identical. Appendix G details the results of the investigation of the differences.

Also, as part of the investigation into the discrepancies between the NASA results and the results of this study, the 15-minute rime shape was used in an investigation of possible conduction errors due to non-uniform initial temperature distribution on the model's surface. It was particularly difficult to achieve a uniform initial surface temperature on this model due to the relatively sharp curvature of the leading edge and the flat surface from the leading edge to the cylinder. A series of modifications were made to the heating arrangement to achieve a more uniform temperature. The subject is discussed in detail in Appendix A. The conclusion of Appendix A is that for the conditions studied

(convective heating arrangement, an average initial skin temperature of approximately 290°F, and the range of variation of skin temperatures of 42°F, 17°F, and 12°F) there was little affect on the results. Nevertheless it was considered wise to have a uniform initial surface temperature distribution (less than 20 °F variation) to eliminate a possible source of errors (i.e. reduce the possibility of conduction errors).

The results of the 15 minute rime ice shape with a smooth surface are given in Figure 15 and in Table 8 in Appendix E. The Nusselt number at the stagnation point was relatively low. The Nusselt number peaked at a point on the highly curved portion (near thermocouple number 4) of the leading edge downstream from the stagnation point. From there it dropped sharply and then remained constant along the flat portion of the model. Tufts were placed on the model to give a visual indication of the flow and it was observed that there was no boundary layer separation from the model for all Reynold's numbers tested.

To determine the effect of leading edge roughness, the same model was tested with a 0.125 inch strip of 60 grit sandpaper (3M 50R4 Garnet Paper Dwt. Open Coat) running spanwise between thermocouples 6 and 7. The results are given in Figure 16 and in Table 9 in Appendix E. The results at thermocouples 6 and 7 are not valid due to the influence of the sandpaper on the thermal mass in that area so they have not been reported. The roughness created turbulence had a significant affect on the heat transfer. At thermocouple 8 the Nusselt number was more than 3 times higher than it had been for the smooth surface case which indicated a high degree of turbulence. Further downstream, the Nusselt number smoothly dropped down to the level of the smooth surface case indicating that the turbulence was being damped out.



Results for the ice shape with roughness "B" are given in Figure 16 and in Table 10 in Appendix E. The Nusselt numbers near the stagnation point were not much different than those for the smooth surface. As the curvature of the leading edge was passed the Nusselt number jumped up to a high value as was the case when the sandpaper strip was used. With roughness "B", however, the Nusselt numbers were higher for all downstream points.

Results for the ice shape with roughness "D", given in Figure 16 and in Table 11 in Appendix E, were similar to the results with roughness "B". The peak in Nusselt number occurred at a slightly upstream location compared to roughness "B", possibly due to the greater roughness height. The drop in Nusselt numbers downstream of the peak was more than that for roughness "B", which could have been due to a thickening of the boundary layer as was mentioned in the results for the cylinder tests.

#### 2-Minute Glaze Ice Shape

The shape for 2 minutes of glaze ice accumulation is shown in Figure 17 with coordinates given in Table 2. The results for this shape with a smooth surface are given in Figure 18 and Table 12 in Appendix E. As was expected the results were similar to the results of the circular cylinder which is similar in shape. The Nusselt numbers near the stagnation point were lower than those for the circular cylinder. It is believed that this is due to the flatness of the shape near the stagnation point. It can be shown using analytical expressions that the Nusselt numbers at the stagnation point of a flat plate perpendicular to the flow will be less than that for a circular cylinder at similar Reynolds numbers.

This model was tested with a 0.125 inch strip of 60 grit sandpaper running span-wise between thermocouples 3 and 4 (the results are not reported for 3 and 4) to make the boundary layer turbulent. The results appear in Figure 19 and Table 13 in Appendix E. There was a peak in the Nusselt numbers just past the strip. Otherwise the results are similar to the smooth surface case.

Results for the ice shape with roughness "B" are given in Figure 19 and in Table 14 in Appendix E. The results were similar to the results for the circular cylinder with roughness "B". The remarks made earlier regarding the Nusselt numbers near at the stagnation point also apply to this case. One further observation is that the roughness did not greatly affect the heat transfer near the stagnation point.

Results for the ice shape with roughness "D" are given in Figure 19 and Table 15 in Appendix E. The results were similar to those for roughness "B" with a slightly extended region of high heat transfer rate.

#### 5-Minute Glaze Ice Shape

The shape for 5 minutes of glaze ice accumulation is shown in Figure 20 with coordinates given in Table 3. It was not always possible to form the skin precisely, as was evident in this model. The line connecting the stagnation point to the center of the circular wooden cylinder on which the skin was mounted was approximately  $3^\circ$  from perpendicular to the front surface of the model. The model was mounted in the wind tunnel so that the front surface was perpendicular to the air flow and it was assumed that the  $3^\circ$  that the model had to be rotated to achieve perpendicularity did not affect the data.

The results for the 5-minute glaze shape with a smooth surface are given in Figure 21 and Table 16 in Appendix E. As can be seen there were peaks in the Nusselt number on the convex portion of the surface. The concave portions of the surface including the stagnation point had relatively low Nusselt numbers. The ice shape formation is at least partially a result of the circumferential distribution of heat transfer so it was not surprising to find high heat transfer rates in areas of greater ice build-up.

This model was tested with a 0.125 inch strip of 60 grit sandpaper running span-wise on the surface between thermocouples 3 and 4 (the results for 3 and 4 are not reported) to make the boundary layer turbulent. The results are given in Figure 22 and in Table 17 in Appendix E. The results were similar to those for the smooth surface case with a much higher Nusselt number peak.

Results for the ice shape with roughness "B" are given in Figure 22 and in Table 18 in Appendix E. The results were similar to the smooth surface case with greatly increased maximum Nusselt number.

Results for the ice shape with roughness "D" are given in Figure 22 and in Table 19 in Appendix E. The results were similar to the roughness "B" case with increased Nusselt number everywhere except at the stagnation point.

#### 15-Minute Glaze Ice Shape

The shape for 15 minutes of glaze ice accumulation is shown in Figure 23 with coordinates given in Table 4. As was the case for the 5 minute glaze ice shape the model for this shape had to be rotated about  $3^\circ$  in the wind-tunnel so that the front surface would be perpendicular to the air flow.

The results for 15-minute glaze shape with a smooth surface are given in Figure 24 and Table 20 in Appendix E. The comments made for the 5 minute glaze shape concerning the Nusselt number peaks and the ice shape also apply to this model. One observation that needs to be made but is not obvious in Figure 24 is that there was apparently a very high peak in the heat transfer near thermocouple 9. As mentioned in the Data Reduction section, at points of maximum heat transfer the indicated Nusselt number would peak at some time soon after injecting the model into the wind tunnel. This was not the case for thermocouple 9. For thermocouple 9 the Nusselt numbers continued to rise as time passed after injection. Also, the plots of

$\ln \left( \frac{T_i - T_R}{T - T_R} \right)$  versus time indicated increasing amounts of conduction out of the area around thermocouple 9 as time increased. Both of these conditions could have resulted from a high peak in Nusselt number near thermocouple 9 but not at thermocouple 9, thus the conclusion that there was a high peak nearby.

Figure 25 and Table 21 in Appendix E give results for tests run with a 0.125 inch strip of 60 grit sandpaper running span-wise on the surface between thermocouples 7 and 8 to make the boundary layer turbulent. This location for the strip was chosen because it was upstream of the region of maximum heat transfer. It was recognized that due to the expected air flow pattern around the model, placement of the strip nearer to thermocouple 9 would have been desirable. But it was more desirable not to have the strip affect the thermal mass at thermocouples 8 and 9. Further, it was felt that there was significant space between 7 and 8 to prevent the sandpaper from affecting their thermal mass. The only significant difference between these results and those for the smooth surface were increased

heat transfer just past the strip of sandpaper. Heat transfer at the other positions was apparently unaffected.

Figure 25 and Table 22 in Appendix E give results for this shape with roughness "B". Roughness "B" seemed to decrease the heat transfer except at the peaks where it was greatly increased. The heat transfer past the peak was only slightly affected because the air flow is separated from the model in this region.

Figure 25 and Table 23 in Appendix E give results for this shape with roughness "D". The results were essentially the same as for the case with roughness "B". There was increased heat transfer compared to roughness "B" in the separated region downstream of the peak, possibly due to the significant roughness height.

## CHAPTER IV

### CONCLUSIONS

The objective of the study was to determine the local convective heat transfer coefficients for ice shapes. At the present, heat transfer coefficients for circular cylinders are used in analytical work for ice shapes. It was felt that the coefficients for ice shapes would be significantly different from those of circular cylinders. Thus, there was a need for the measurement of heat transfer coefficients of ice shapes. Four ice-shape models were tested with varying degrees of surface roughness.

The thin-skin heat rate technique was chosen as the method of measuring the heat transfer rates. It was validated by comparing  $Nu$  measured for a circular cylinder model with the  $Nu$  predicted by the analytical expression derived by Frossling. Agreement between the measured  $Nu$  and predicted  $Nu$  was within  $\pm 15\%$ .

The 2-minute glaze ice shape, which was similar to the circular cylinder in shape, had  $Nu$  similar to those for a circular cylinder. The front of the 2-minute glaze ice shape near the stagnation point was flat.  $Nu$  near the stagnation point on a flat plate perpendicular to the flow are constant for a given  $Re$  and they were constant on the flat portion of the ice shape. This suggests that the  $Nu$  trend could have been predicted intuitively knowing the trends for a flat plate and a circular cylinder. No attempt was made to relate the magnitudes of the  $Nu$  measured for the ice shape to the magnitudes of the  $Nu$  predicted for a flat plate or circular cylinder. Roughness increased the maximum  $Nu$  by 100% but the minimum  $Nu$  were virtually unchanged.

The shapes for greater amounts of ice accretion were very different from a circular cylinder, but their Nu trends could have been predicted intuitively. Both the 5-minute and 15-minute glaze ice shapes had Nu peaks in regions where the surface was convex and dips in the Nu in regions where the surface was concave. The maximum Nu occurred on the "horns" of the glaze ice shapes and on the curvature of the leading edge of the rime ice shape. The effect of roughness was different for the glaze and rime ice shapes. On the glaze ice shapes roughness increased the maximum Nu by 80% but the other Nu were virtually unchanged. On the rime ice shape the Nu near the stagnation point were unchanged. The maximum Nu was increased by 45%, but the Nu downstream of the peak were increased by approximately 150%. The roughness changed the Nu distribution from one with a sharp peak to one with a step that tapered off in the downstream direction.

An important point that should be made about this study is that the Nu were measured for four specific ice shapes and no attempt was made to generalize the results to apply to other shapes of similar geometry. It would be beneficial in future studies of the convective heat transfer on ice shapes to investigate the effect on Nu of small changes in the geometry of the ice shapes.

## LIST OF REFERENCES

1. Lake, H. B. and Bradley J., "The Problems of Certifying Helicopters for Flight in Icing Conditions", *Aeronautical Journal*, Vol. 80, 1976, pp. 419-433.
2. Korkan, K. D., "Performance Degradation of Propeller/Rotor Systems Due to Rime Ice Accretion", unpublished document of the Ohio State University Aeronautical and Astronautical Research Laboratory in Conjunction with the NASA Lewis Research Center Icing Analysis Workshop, March 17, 1981.
3. Messinger, B. L., "Equilibrium Temperature of an Unheated Icing Surface as a Function of Air Speed", *Journal of the Aeronautical Sciences*, January 1953.
4. Lozowski, E. P., Stallabrass, J. R., and Hearty, P. F., "The Icing of an Unheated Non-Rotating Cylinder in Liquid Water Droplet-Ice Crystal Clouds", report of the National Research Council of Canada, February 1979.
5. Achenbach, E., "Heat Transfer from Smooth and Rough Surfaced Circular Cylinders in Cross Flow", proceedings of the Fifth International Heat Transfer conference, Tokyo, p. 229-33, 1974.
6. Boelter, L. M. K., Cherry, V. H., Johnson and Martinelli, R. L., Heat Transfer Notes, New York, McGraw-Hill Publishers, p. 506-8, 1965.
7. Trimmer, L. L., Mathews, R. K. and Buchanan, T. O., "Measurement of Aerodynamic Heat Rates at the AEDC Von Karman Facility", International Congress on Instrumentation in Aerospace Simulation Facilities, September 1973.
8. Hippensteele, S. A., Russell, L. M. and Stepka, F. S., "Evaluation of a Method for Heat Transfer Measurements and Thermal Visualization Using a Composite of a Heater Element and Liquid Crystals", NASA (E-656).
9. Neal, S.E.H.C., "The Development of the Thin-Film Napthalene Mass-Transfer Analogue Technique for the Direct Measurement of Heat-Transfer Coefficients," *International Journal of Heat Mass Transfer*, Vol. 18, pp. 559-567, 1975.



10. Kapur, D. N., and Macleod, N., "The Determination of Local Mass Transfer Coefficients by Holographic Interferometry-I", Int. S. Heat Mass Transfer 17, pp. 1151-62, 1974.
11. Test Article Design Information Handbook AEDC/VKF Wind Tunnels A/B/C, Arvin/Calspan Field Services Inc./AEDC Division, Arnold Air Force Station, Tennessee 37389, May 1981.
12. Frossling, N., NACA TM, 1432, 1958, Engl. Translation.
13. Van Fossen, J., data presented in an unpublished document presented at the NASA Lewis Research Center Icing Analysis Workshop, February 1983.
14. Kays, W. M., "Laminar Flow Heat Transfer to a Gas with Large Temperature Difference," Transactions of the ASME, Journal of Heat Transfer, Vol. 85, pp. 329-338, 1963.
15. Kline, S. J. and McClintock, F. A., "Describing Uncertainties in Single-Sample Experiments," Mechanical Engineering, p. 3, January 1953.
16. Giedt, W. H., "Investigation of Variation of Point Unit-Heat-Transfer Coefficient Around a Cylinder Normal to an Air Stream," Transactions of the ASME, Vol. 71, 1949.

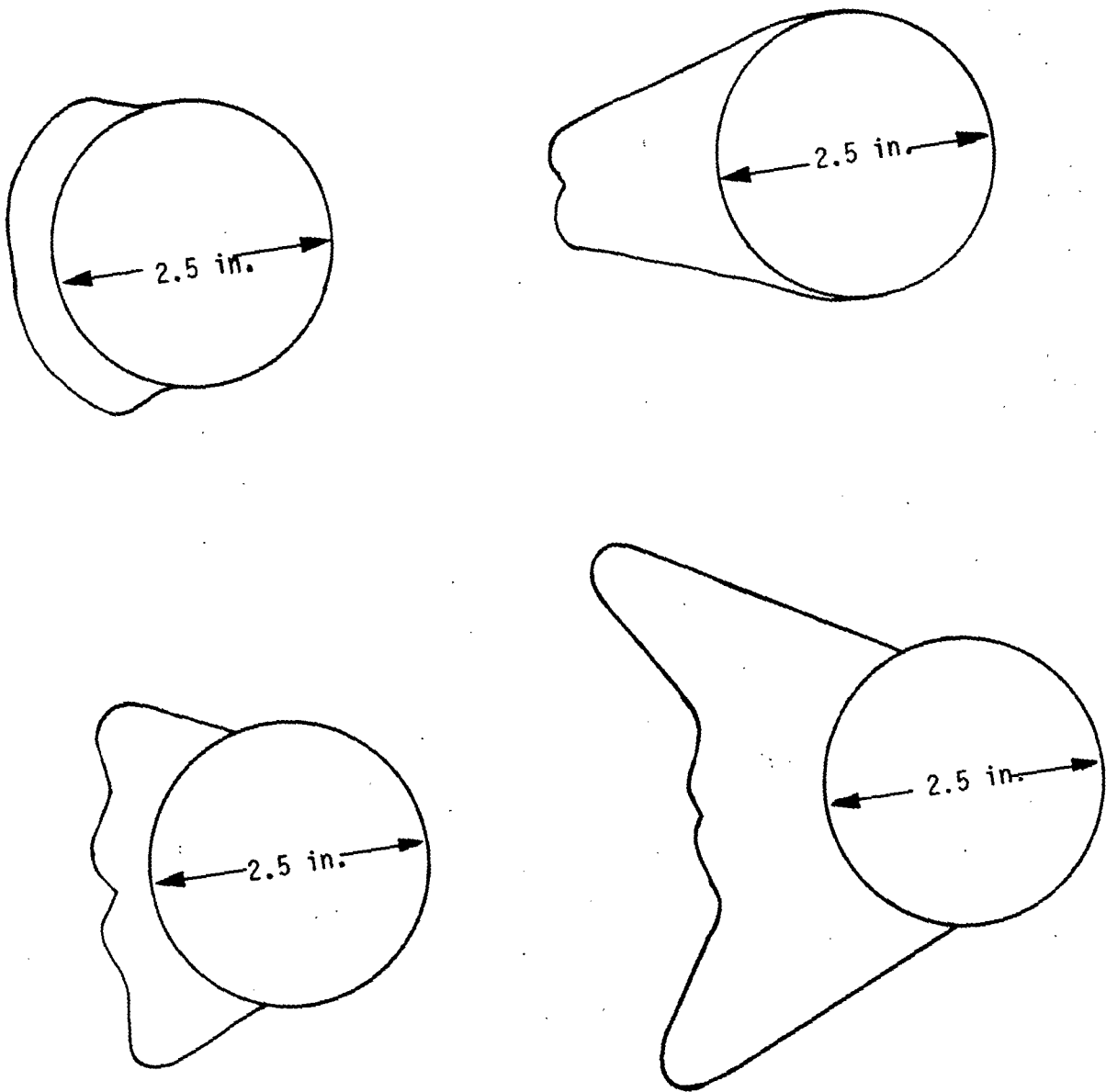


Figure 1. Ice Accretion Shapes.

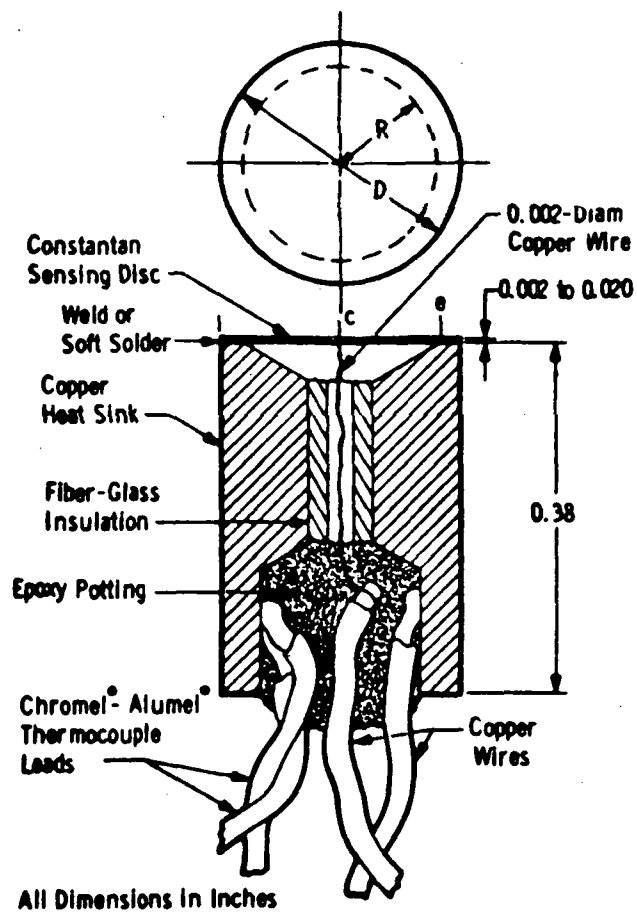


Figure 2. Gardon Gage.

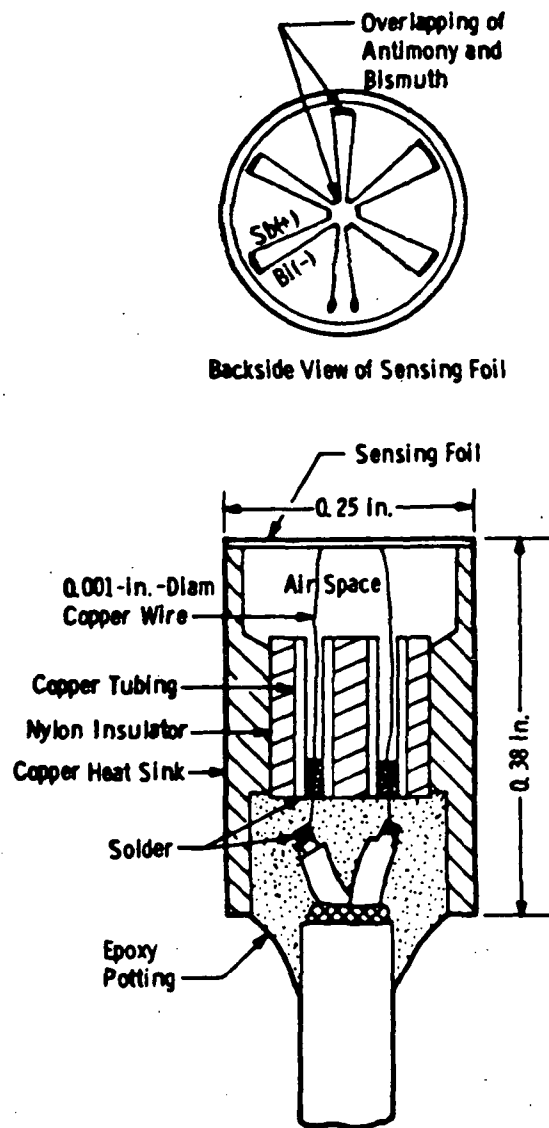


Figure 3. High-Sensitivity Gardon Gage.

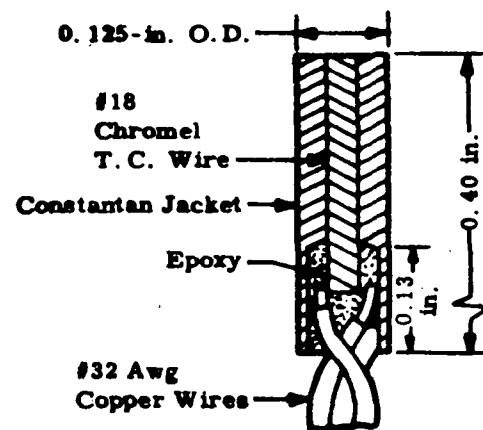


Figure 4. Coaxial Thermocouple Gage.

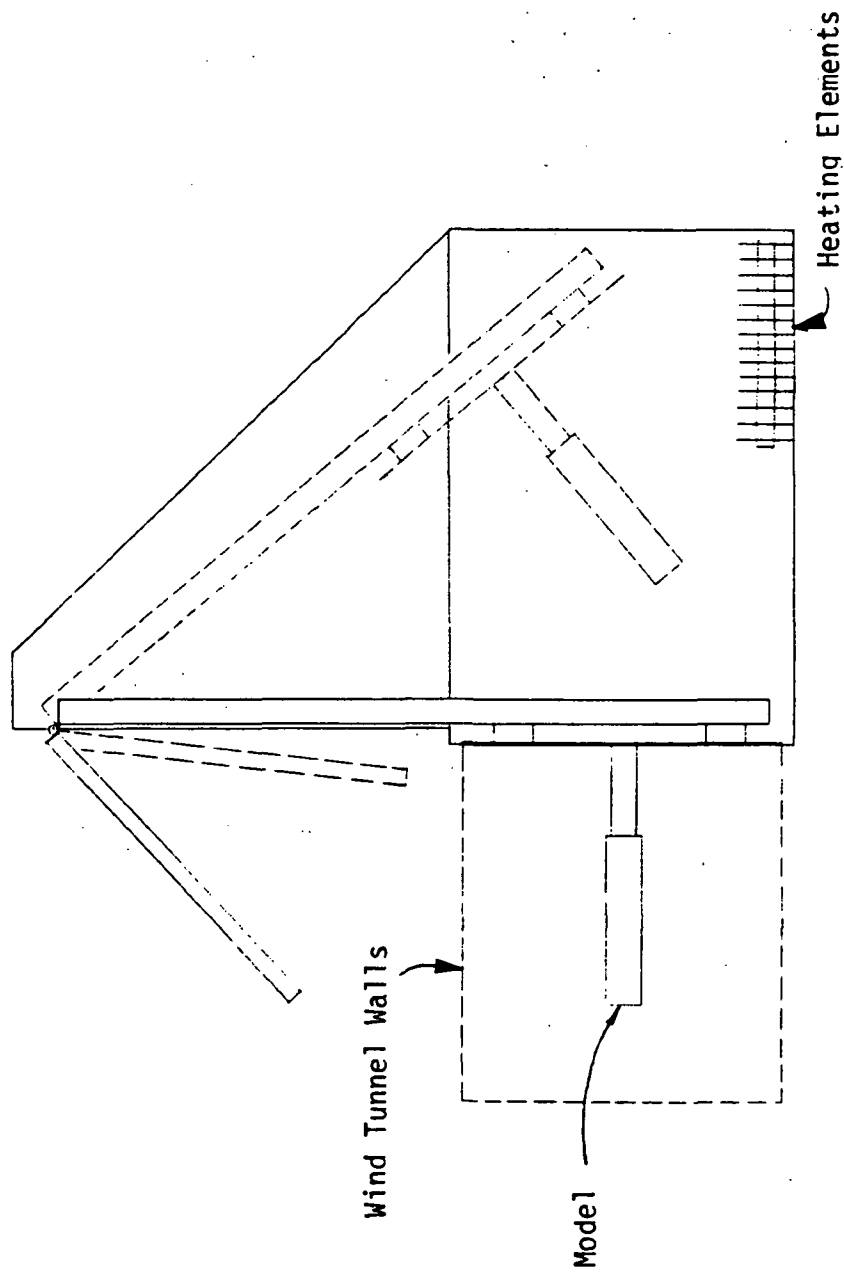


Figure 5. Schematic of the Heating Box.  
View looking forward from a downstream position in the wind tunnel.

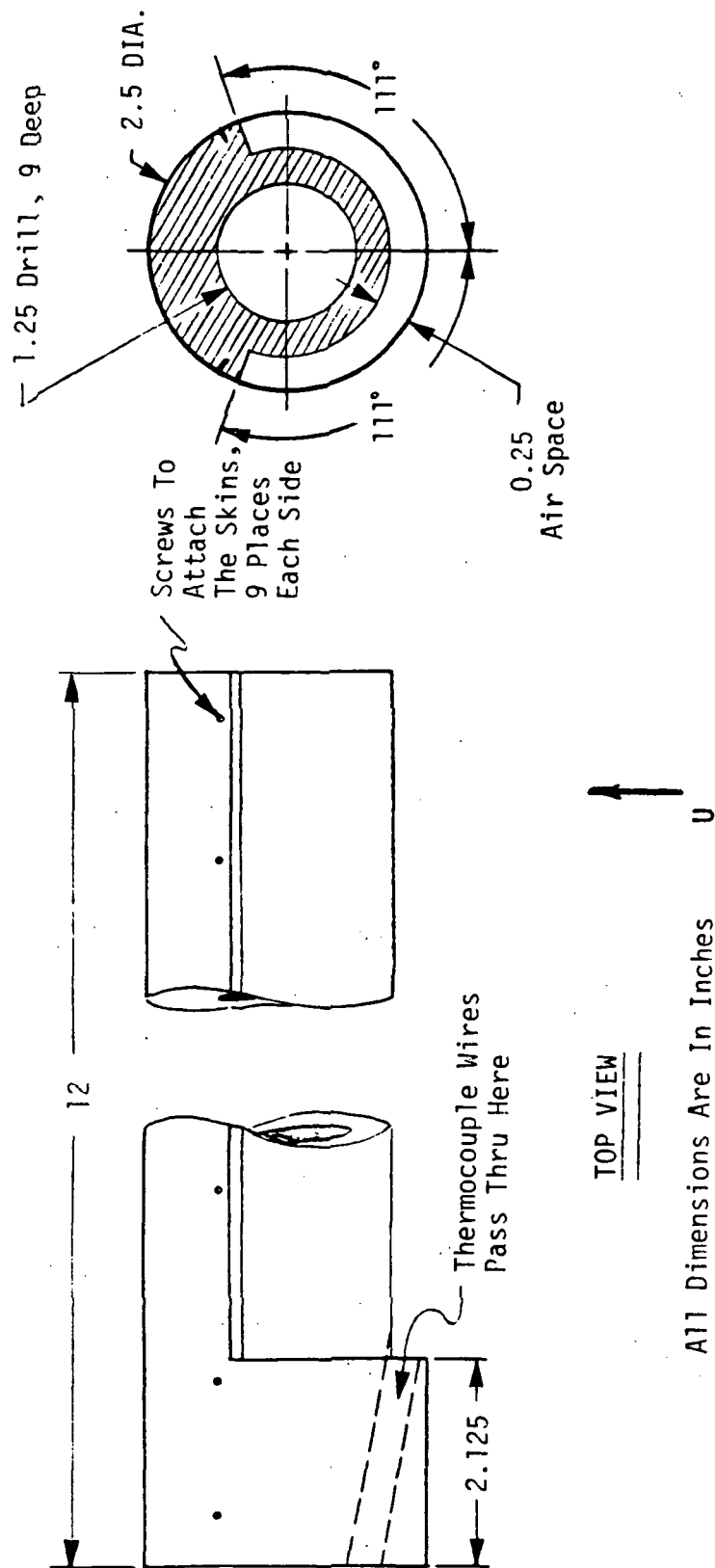


Figure 6. The Model Substructure.

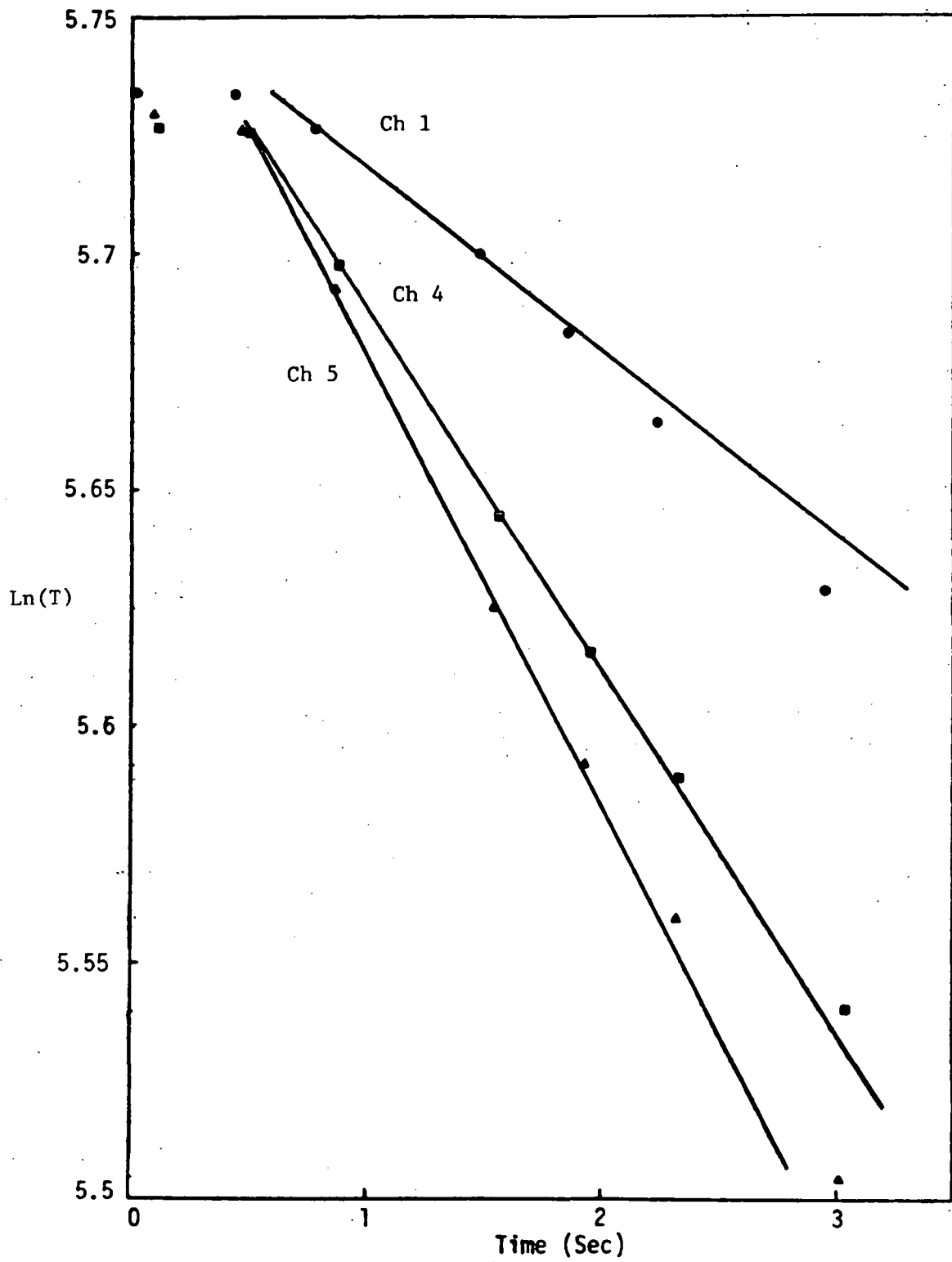


Figure 7. Data for the 15-Minute Rime Shape Showing Non-linearities.



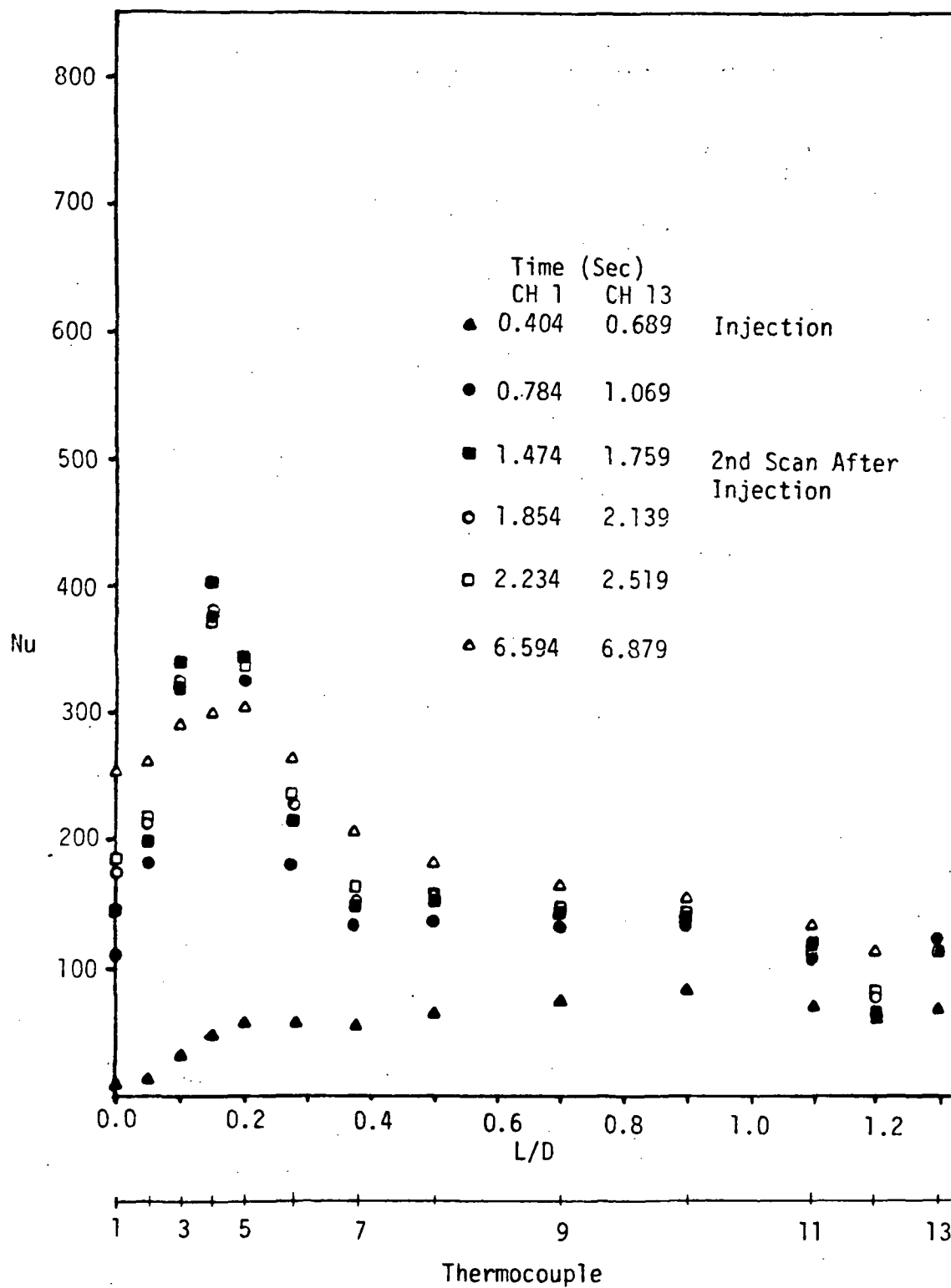
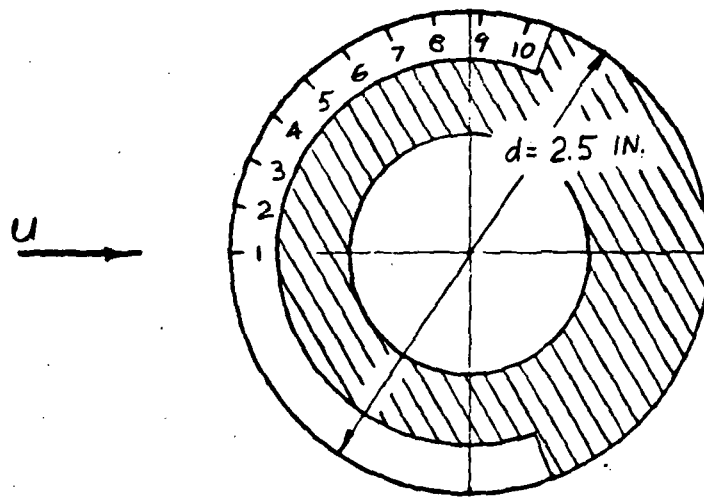


Figure 8. Time Variation of the Nusselt Numbers.



**Figure 9. The Circular Cylinder with Thermocouple Locations.**

The hatched portion represents the wooden cylinder used as a substructure.

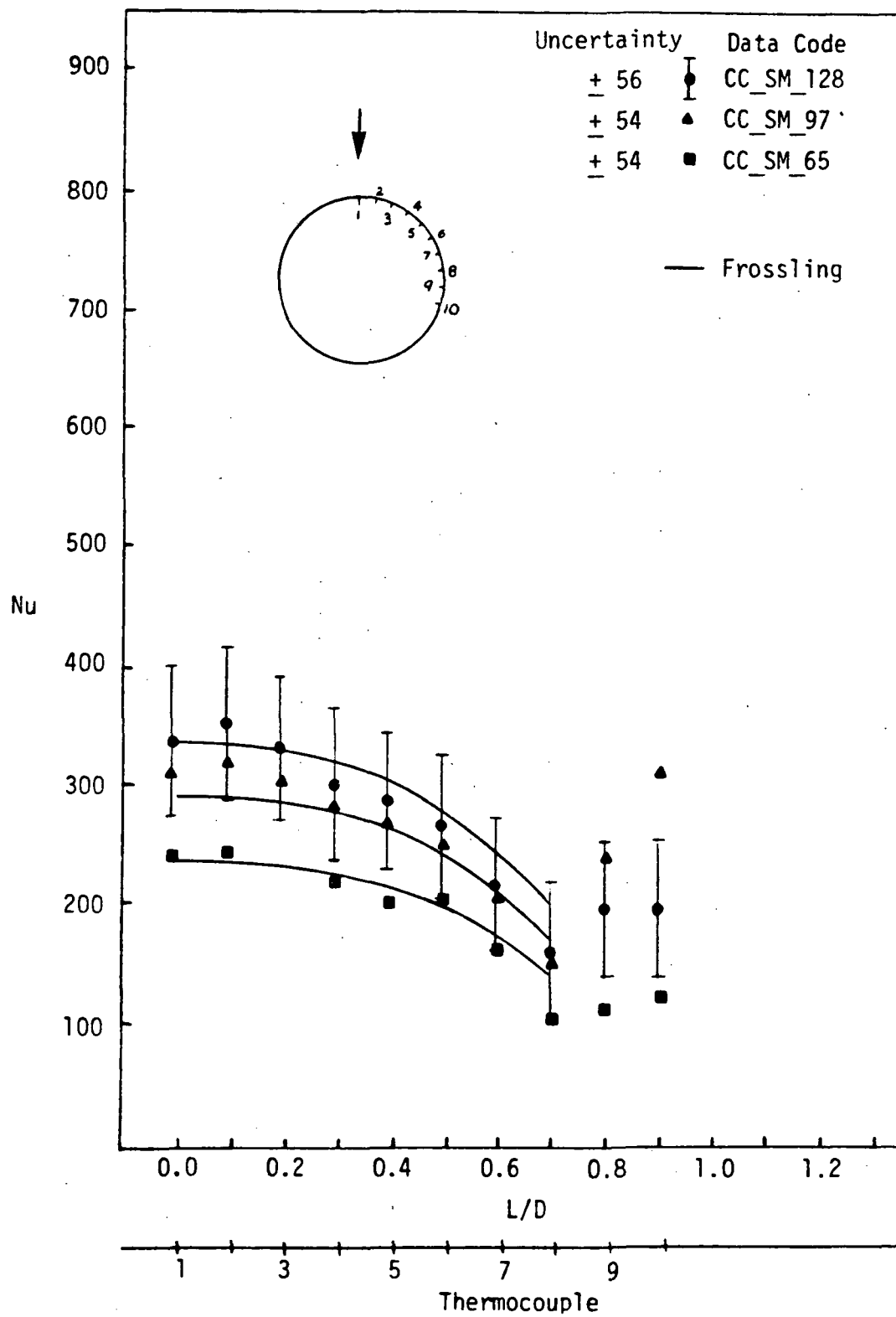


Figure 10. Nusselt Numbers for the Smooth Circular Cylinder.

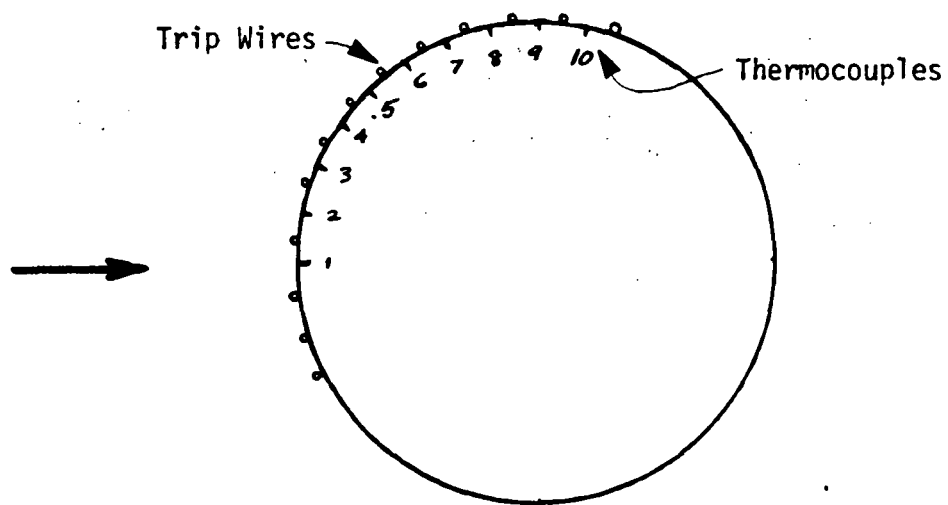
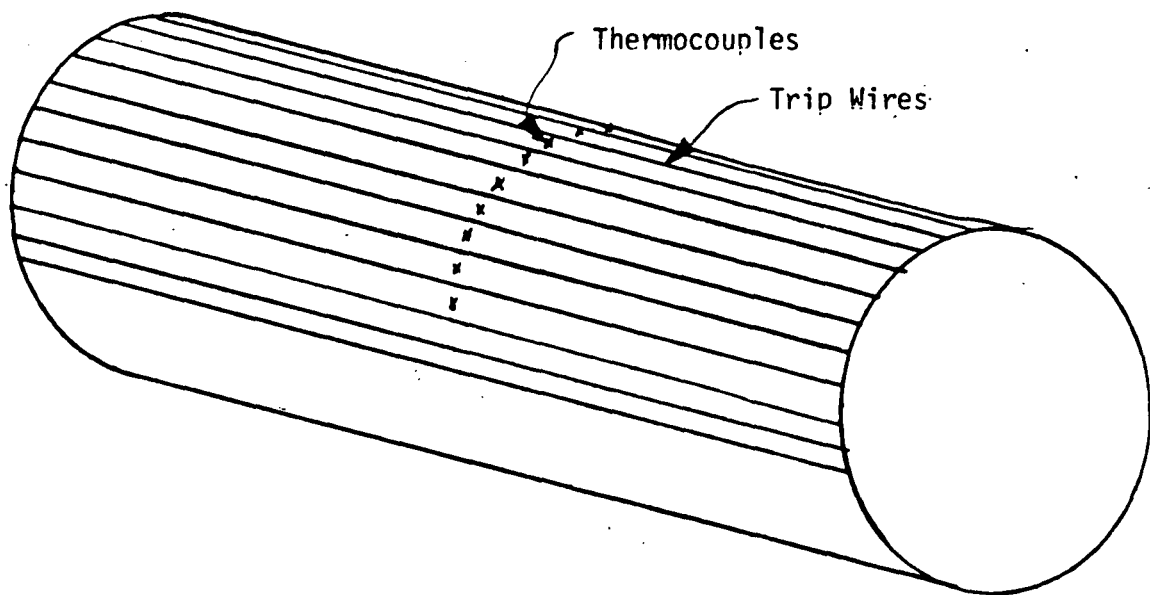


Figure 11. Roughness "B" on the Circular Cylinder.

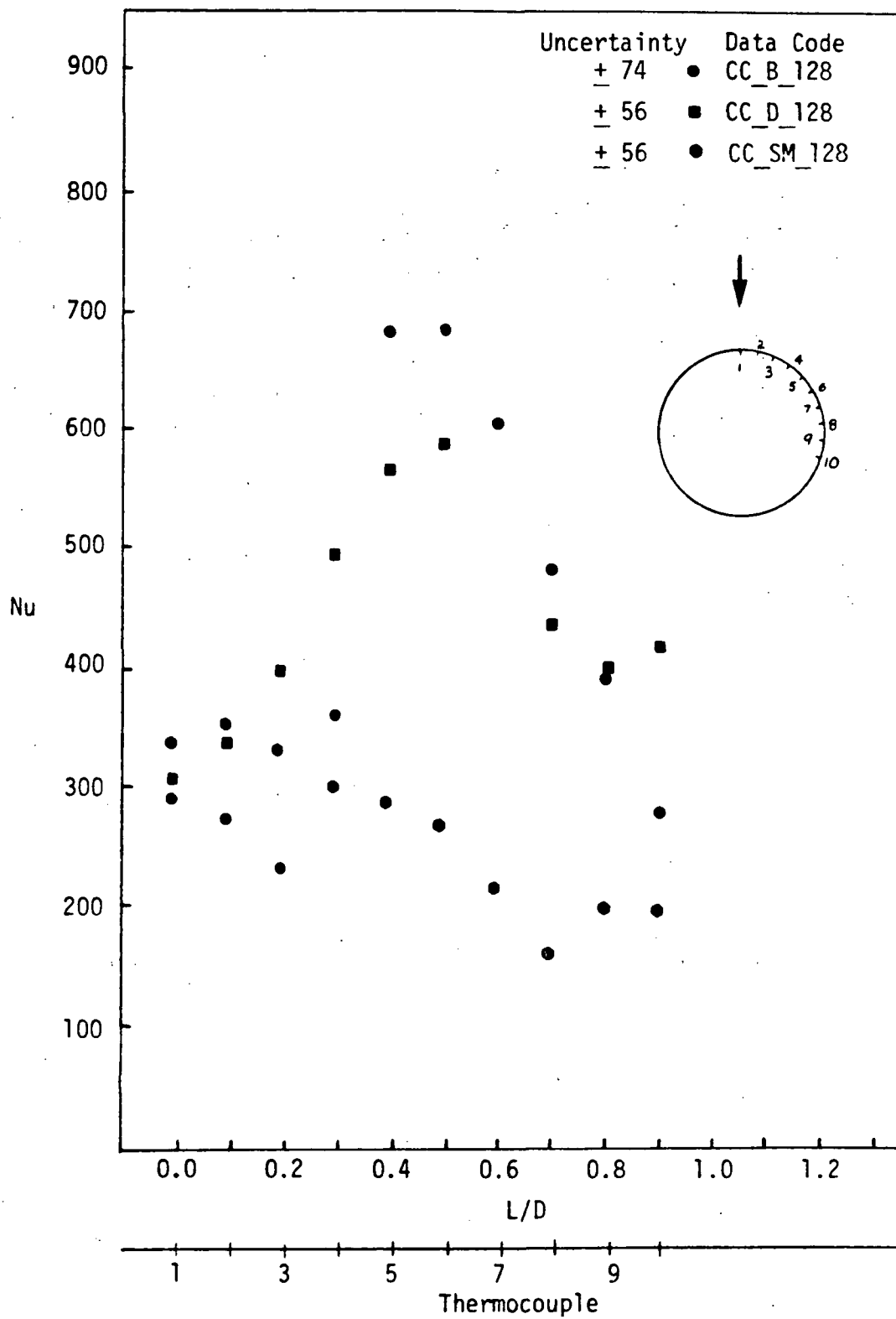


Figure 12. Nusselt Numbers for the Rough Circular Cylinder.

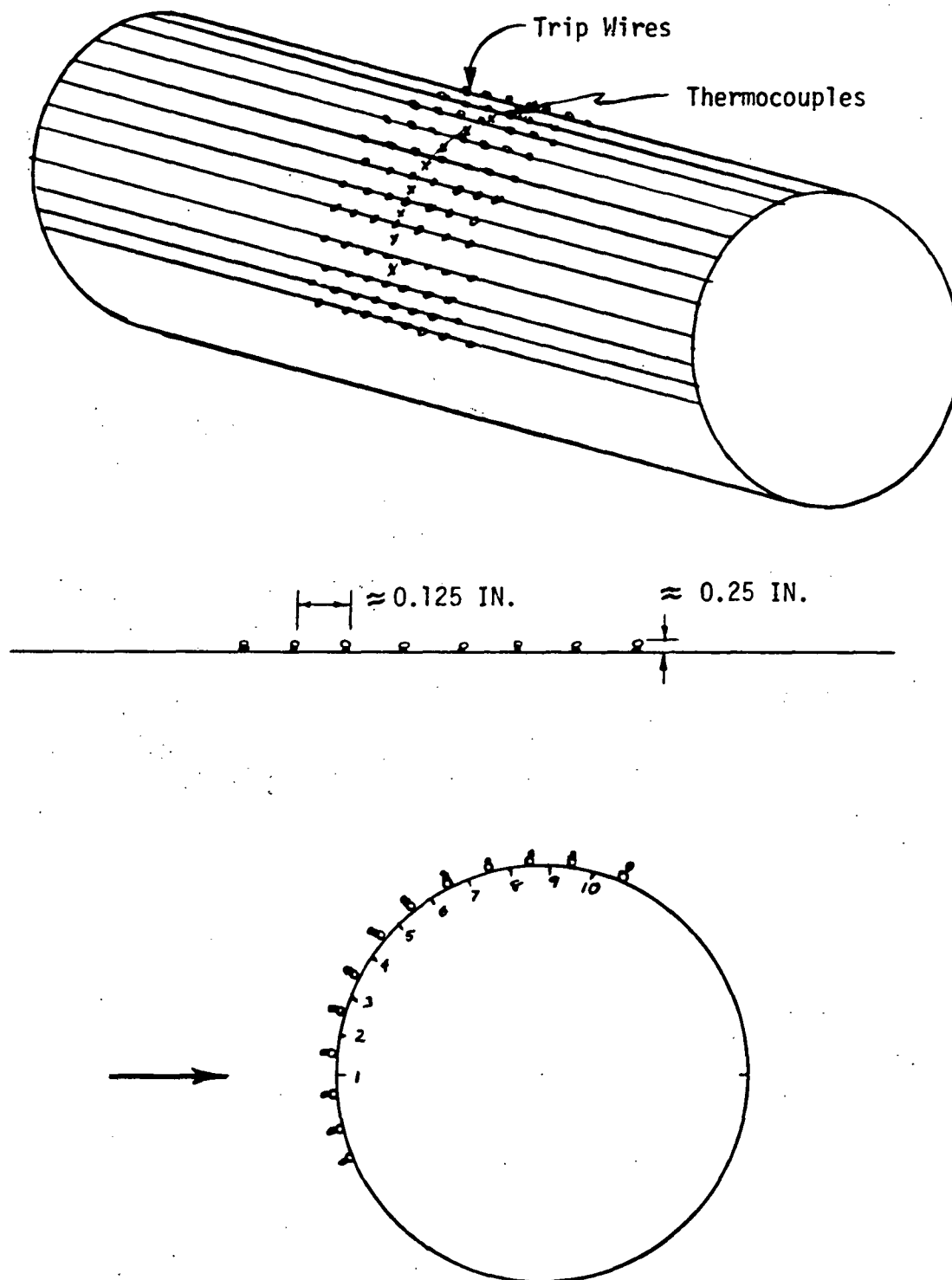


Figure 13. Roughness "D" on the Circular Cylinder.

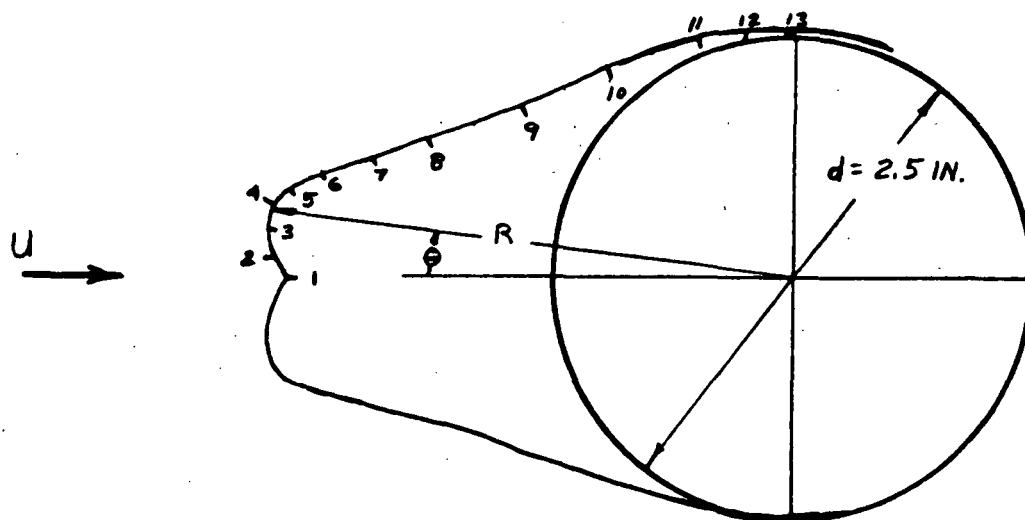


Figure 14. The 15-Minute Rime Ice Shape.

Thermocouple locations are shown. See Table 1 for coordinates.

Table 1. Coordinates for the 15-Minute Rime Shape

$\theta$	R/d	$\theta^\circ$	R/d	$-\theta^\circ$	R/d	$-\theta^\circ$	R/d
0	1.044	45	0.6	2.5	1.068	50	0.552
2.5	1.064	50	0.58	5	1.092	55	0.54
5	1.084	55	0.564	7.5	1.1	60	0.524
7.5	1.088	60	0.552	10	1.084	65	0.52
10	1.06	65	0.544	12.5	1.032	70	0.512
12.5	0.992	70	0.536	15	0.96	75	0.508
15	0.932	75	0.516	20	0.836	80	0.496
20	0.828	80	0.52	25	0.744	85	0.496
25	0.748	85	0.516	30	0.684	90	0.496
30	0.692	90	0.516	35	0.64		
35	0.652			40	0.604		
40	0.62			45	0.576		



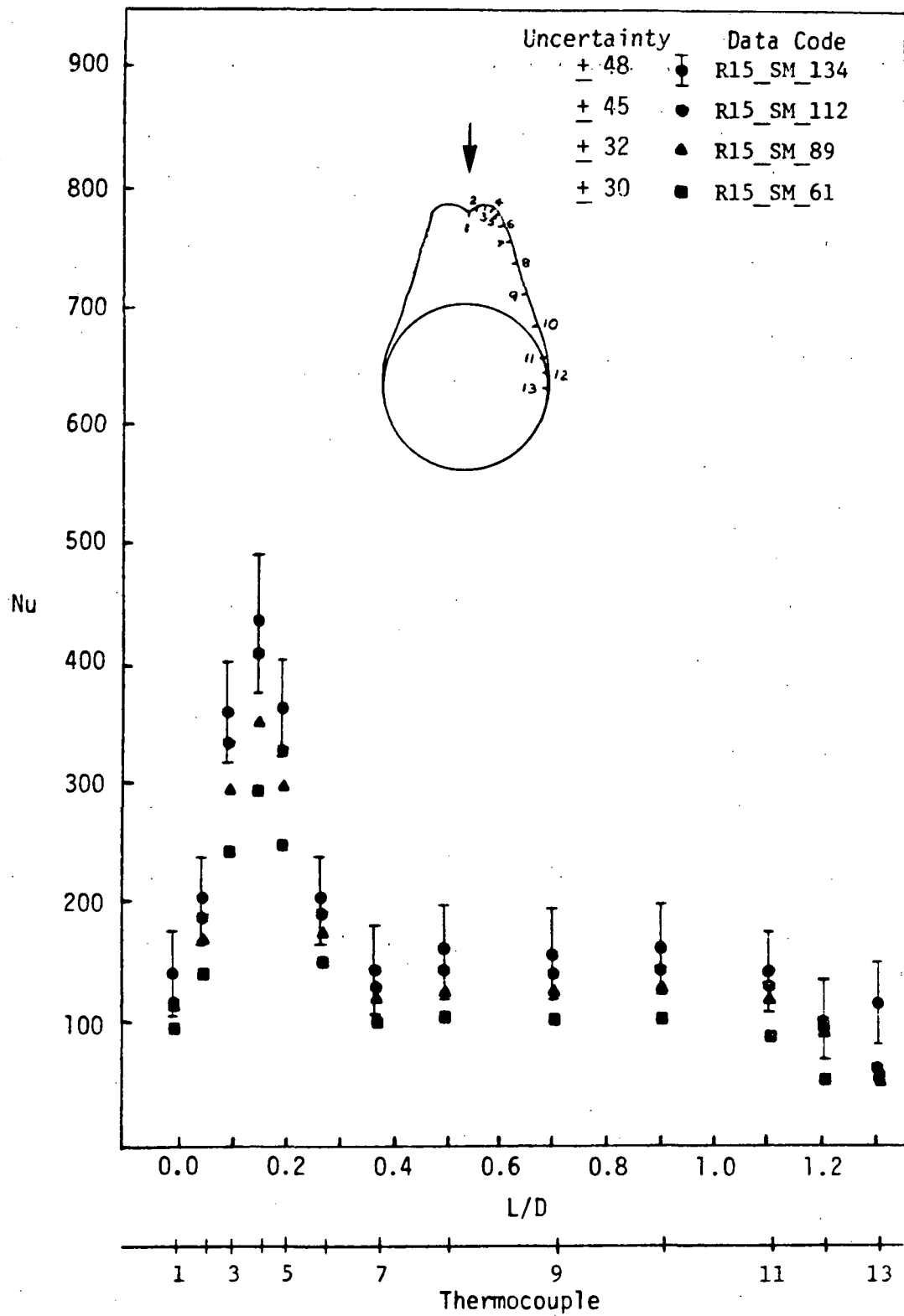


Figure 15. Nusselt Numbers for the Smooth 15-Minute Rime Ice Shape.

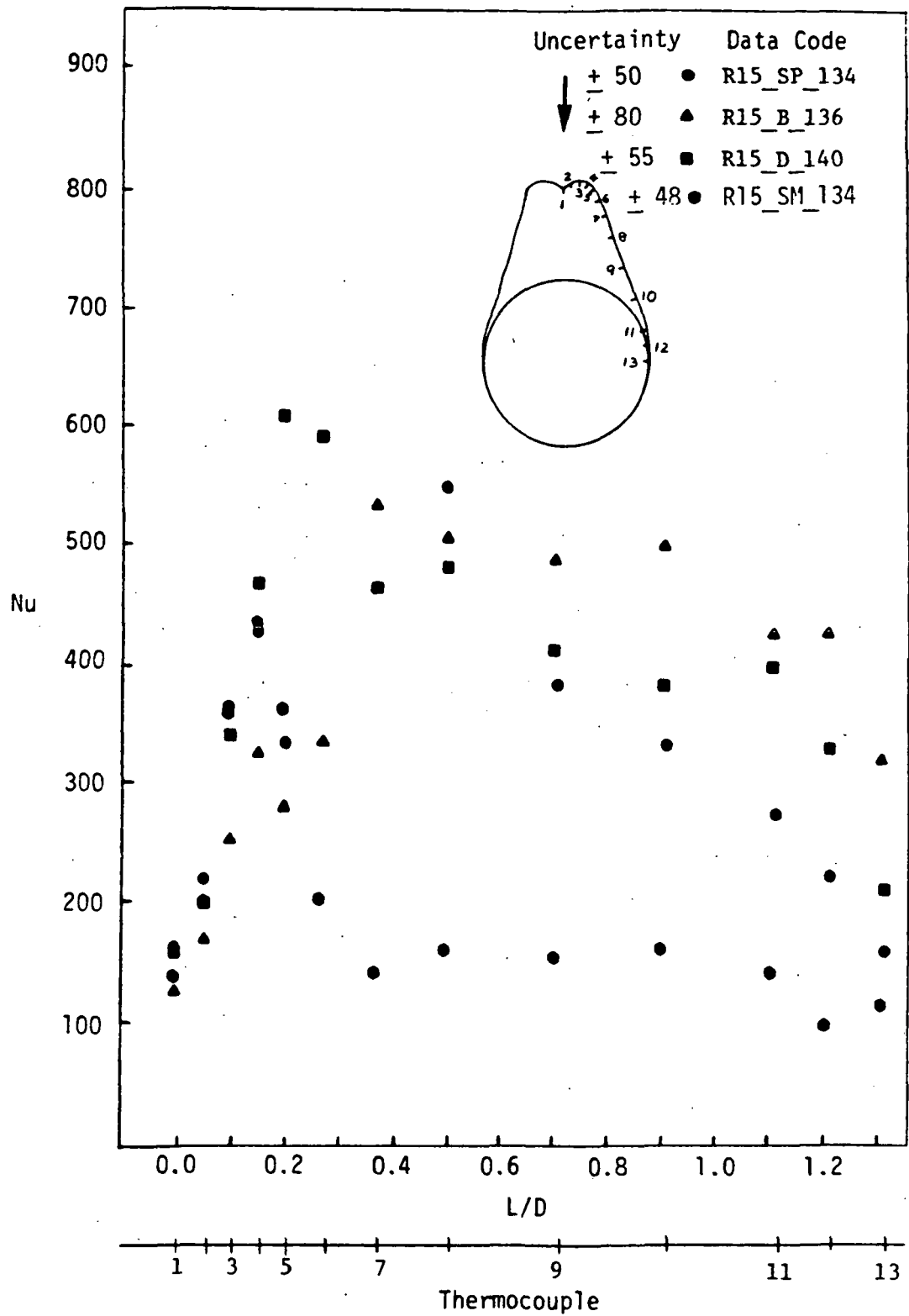


Figure 16. Nusselt Numbers for the Rough 15-Minute Rime Ice Shape.

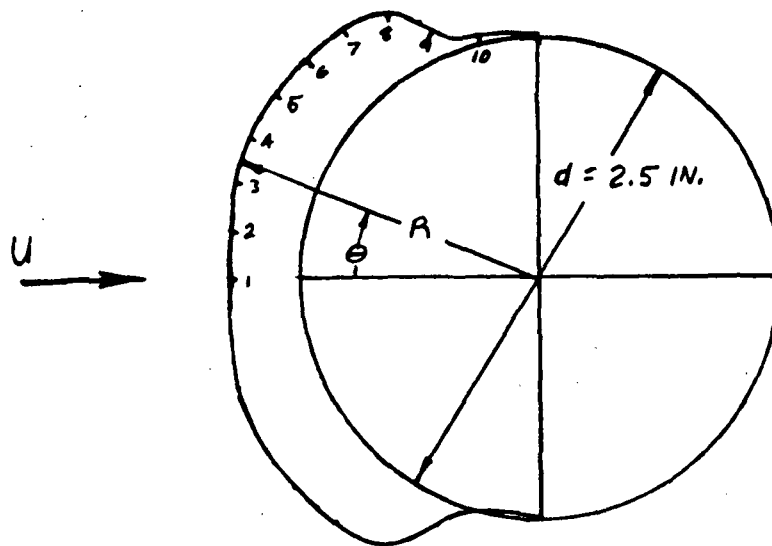


Figure 17. The 2-Minute Glaze Ice Shape.

Thermocouple locations are shown. See Table 2 for coordinates.

Table 2. Coordinates for the 2-Minute Glaze Shape

$\theta$	R/d	$\theta^\circ$	R/d	$-\theta^\circ$	R/d	$-\theta^\circ$	R/d
0	0.644	65	0.584	5	0.644	67.5	0.548
5	0.648	67.5	0.544	10	0.656	70	0.516
10	0.652	70	0.528	15	0.664	72.5	0.504
15	0.66	72.5	0.516	20	0.664	75	0.496
20	0.668	75	0.512	25	0.668	80	0.488
25	0.668	80	0.508	30	0.668	85	0.492
30	0.668	85	0.504	35	0.668	90	0.492
35	0.668	90	0.508	40	0.672	95	0.5
40	0.664	95	0.508	45	0.66		
45	0.664			50	0.66		
50	0.66			55	0.656		
55	0.625			57.5	0.648		
57.5	0.644			60	0.628		
60	0.628			62.5	0.608		
62.5	0.608			65	0.58		

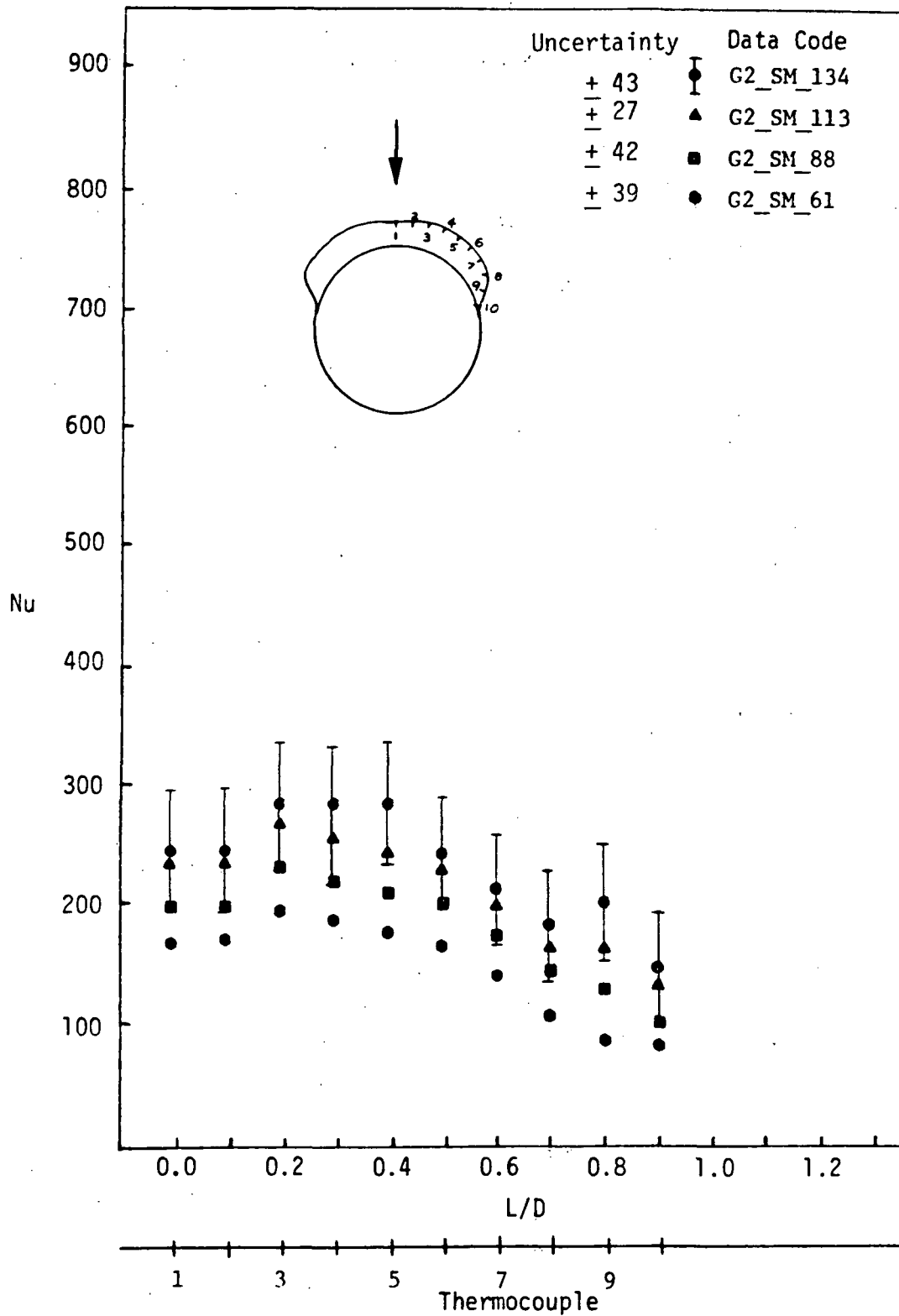


Figure 18. Nusselt Numbers for the Smooth 2-Minute Glaze Ice Shape.

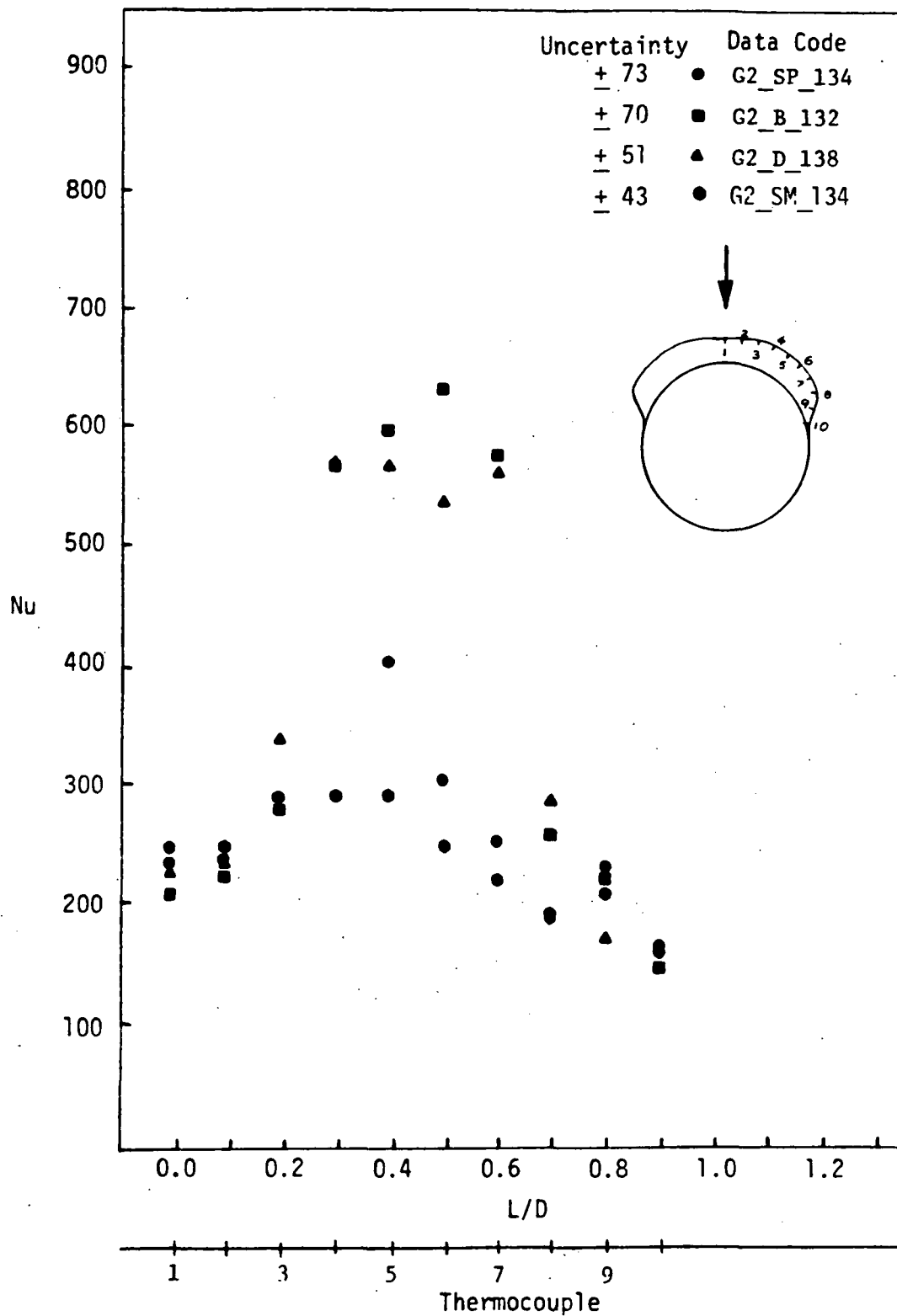


Figure 19. Nusselt Numbers for the Rough 2-Minute Glaze Ice Shape.

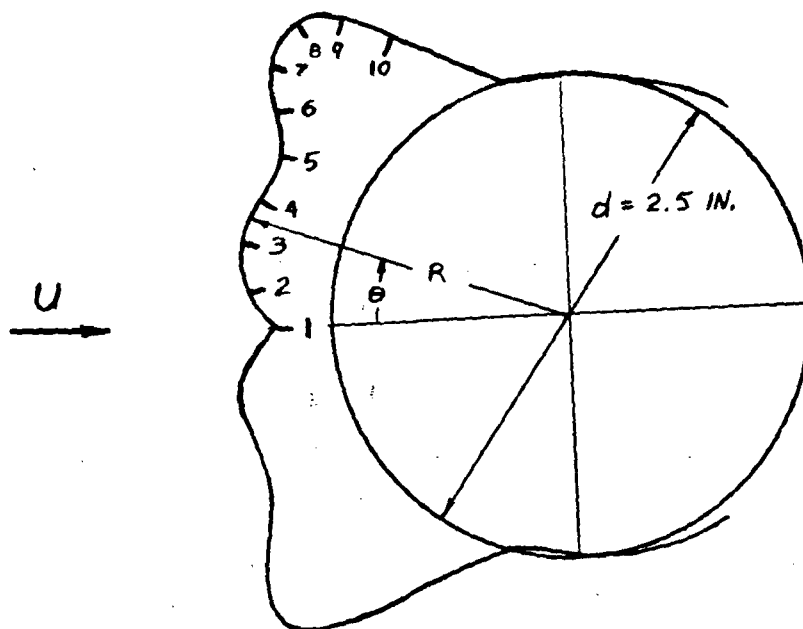


Figure 20. The 5-Minute Glaze Ice Shape.

Thermocouple locations are shown. See Table 3 for coordinates.

**Table 3. Coordinates for the 5 Minute Glaze Ice Shape**

$\theta$	R/d	$\theta$	R/d	$-\theta$	R/d	$-\theta$	R/d
0	0.616	50	0.832	5	0.67	50	0.804
5	0.600	55	0.788	10	0.204	55	0.700
10	0.690	60	0.688	15	0.712	60	0.624
15	0.700	65	0.604	20	0.708	65	0.548
20	0.696	70	0.548	25	0.712	70	0.508
25	0.680	75	0.508	30	0.736	75	0.492
30	0.676	80	0.504	35	0.796	80	0.490
35	0.710	85	0.500	40	0.852	85	0.492
40	0.788	90	0.500	45	0.848	90	0.492
45	0.832						



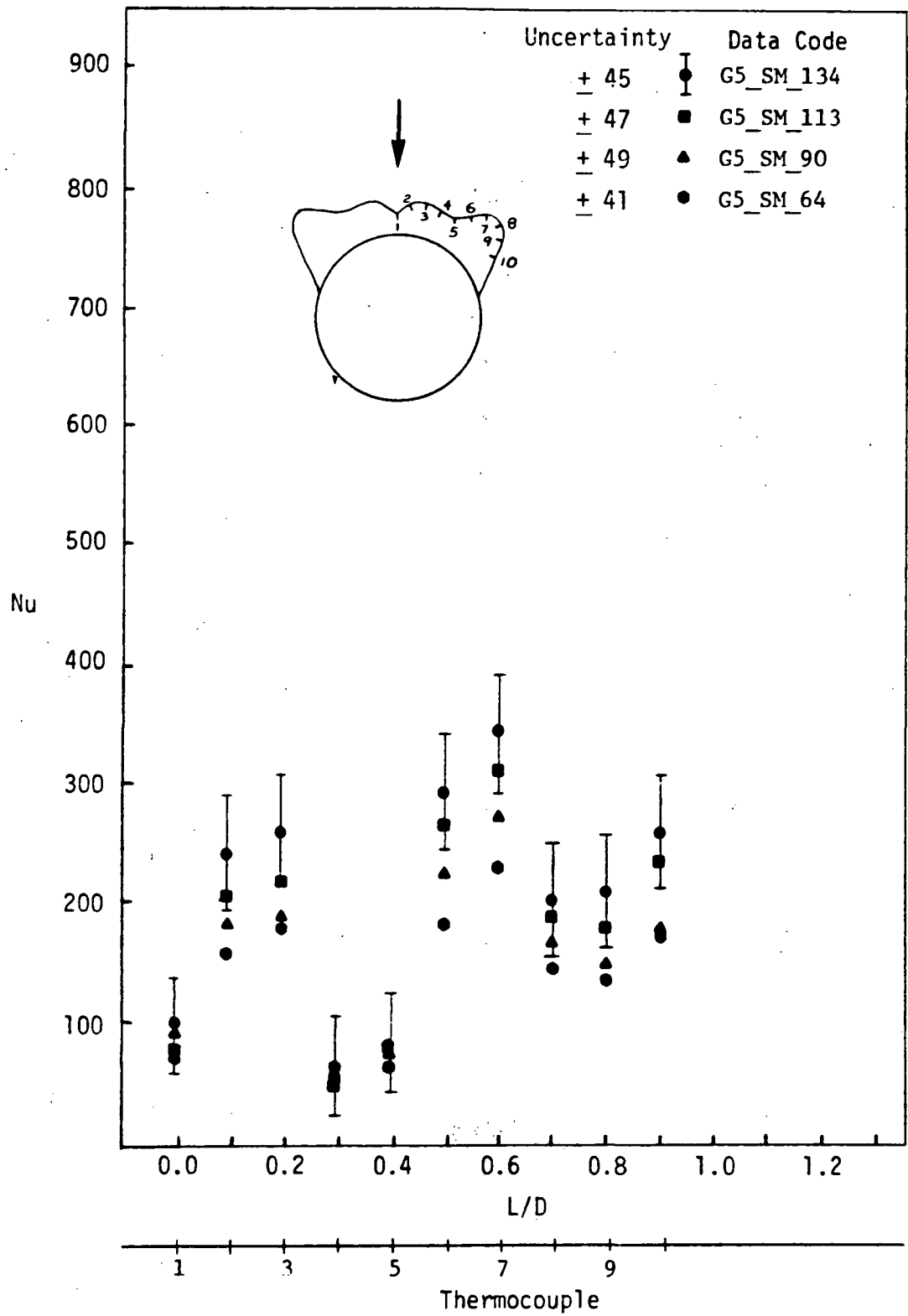


Figure 21. Nusselt Numbers for the Smooth 5-Minute Glaze Ice Shape.

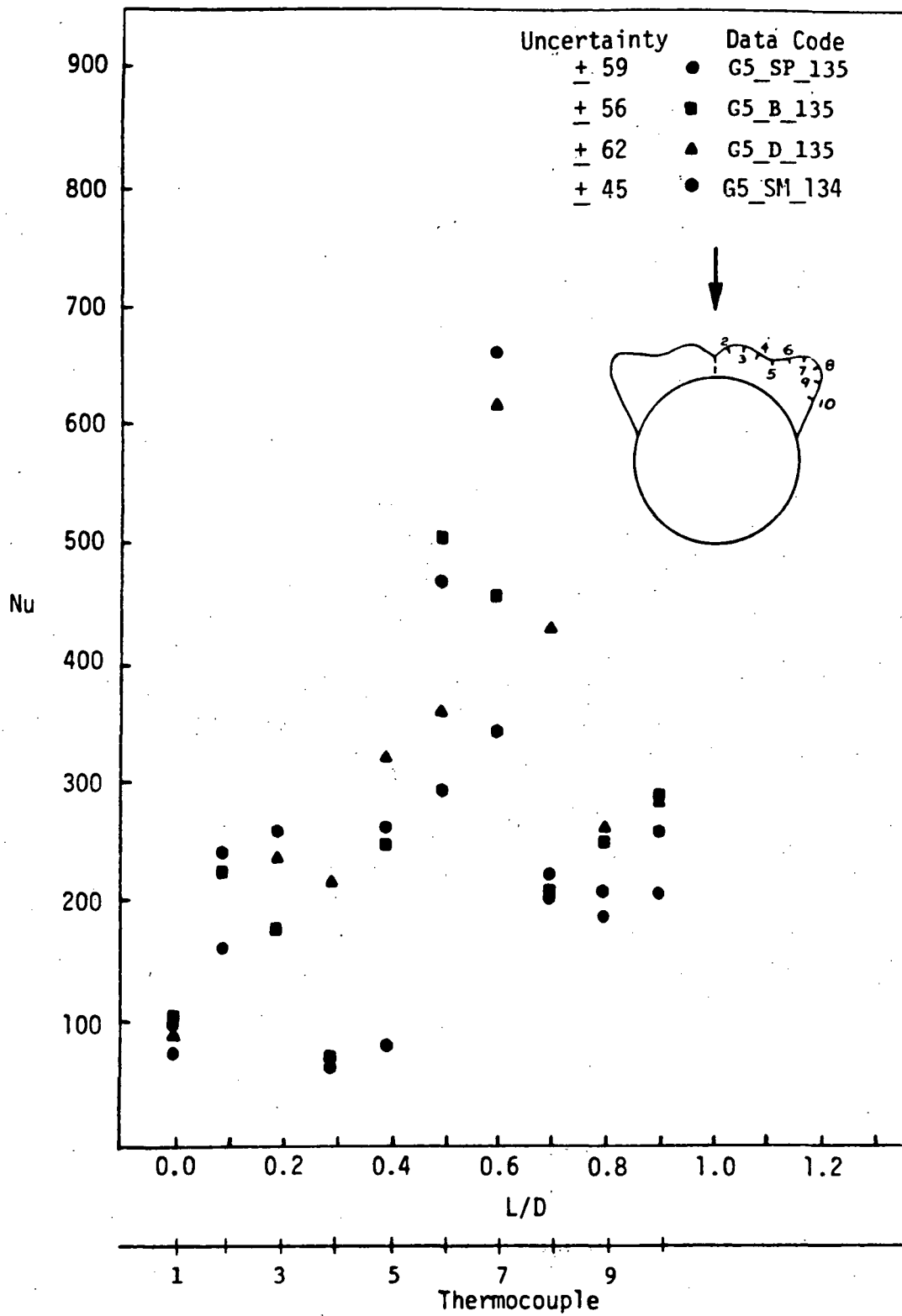


Figure 22. Nusselt Numbers for the Rough 5-Minute Glaze Ice Shape.

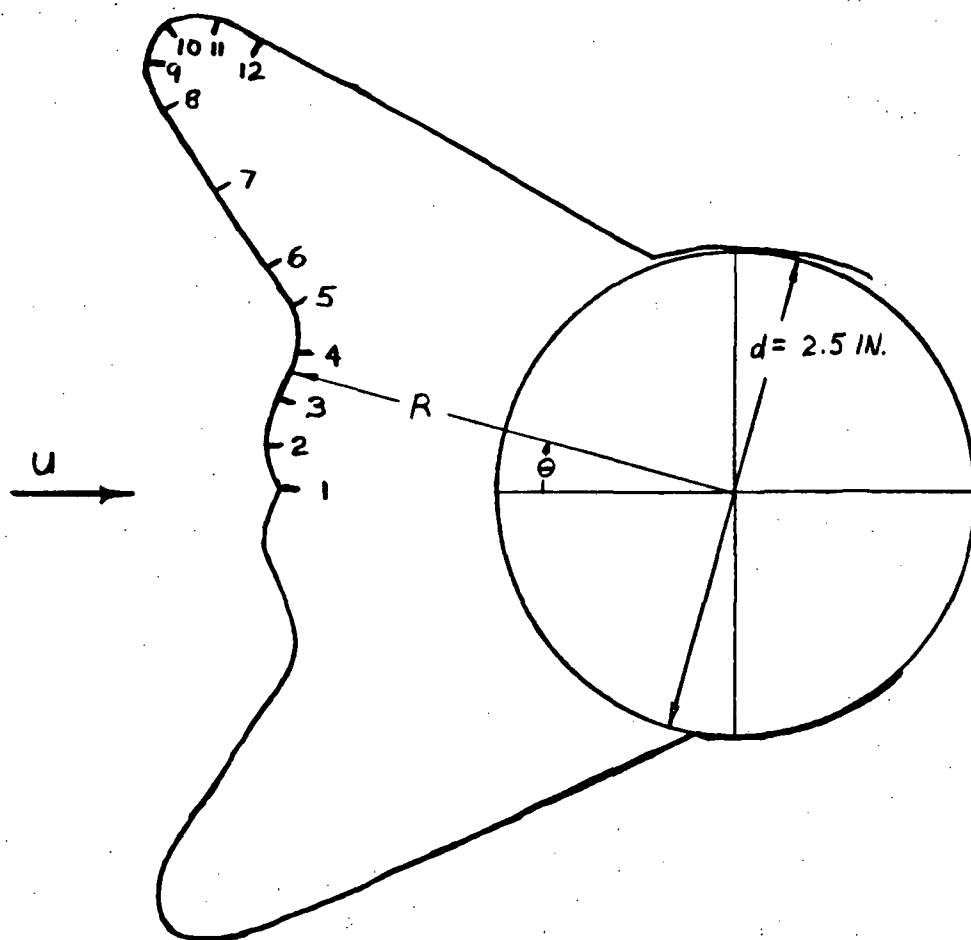


Figure 23. The 15-Minute Glaze Ice Shape.

Thermocouple locations are shown. See Table 4 for coordinates.

**Table 4. Coordinates for the 15-Minute Glaze Shape**

$\theta$	R/d	$\theta$	R/d	$-\theta$	R/d	$-\theta$	R/d
0	0.952	37.5	1.520	2.5	0.968	37.5	1.476
2.5	0.960	40	1.492	5	0.984	40	1.448
5	0.980	42.5	1.372	7.5	0.980	42.5	1.324
7.5	0.984	45	1.228	10	0.976	45	1.204
10	0.972	50	0.968	15	0.960	50	0.988
15	0.952	55	0.752	17.5	0.960	55	0.832
17.5	0.952	60	0.656	20	0.980	60	0.752
20	0.972	65	0.576	22.5	1.020	65	0.656
22.5	1.012	67.5	0.544	25	1.076	67.5	0.624
25	1.072	70	0.520	30	1.260	70	0.596
30	1.260	75	0.508	32.5	1.372	75	0.544
32.5	1.380	80	0.504	35	1.456	80	0.504
35	1.484	85	0.504			85	0.504
		90	0.500			90	0.504

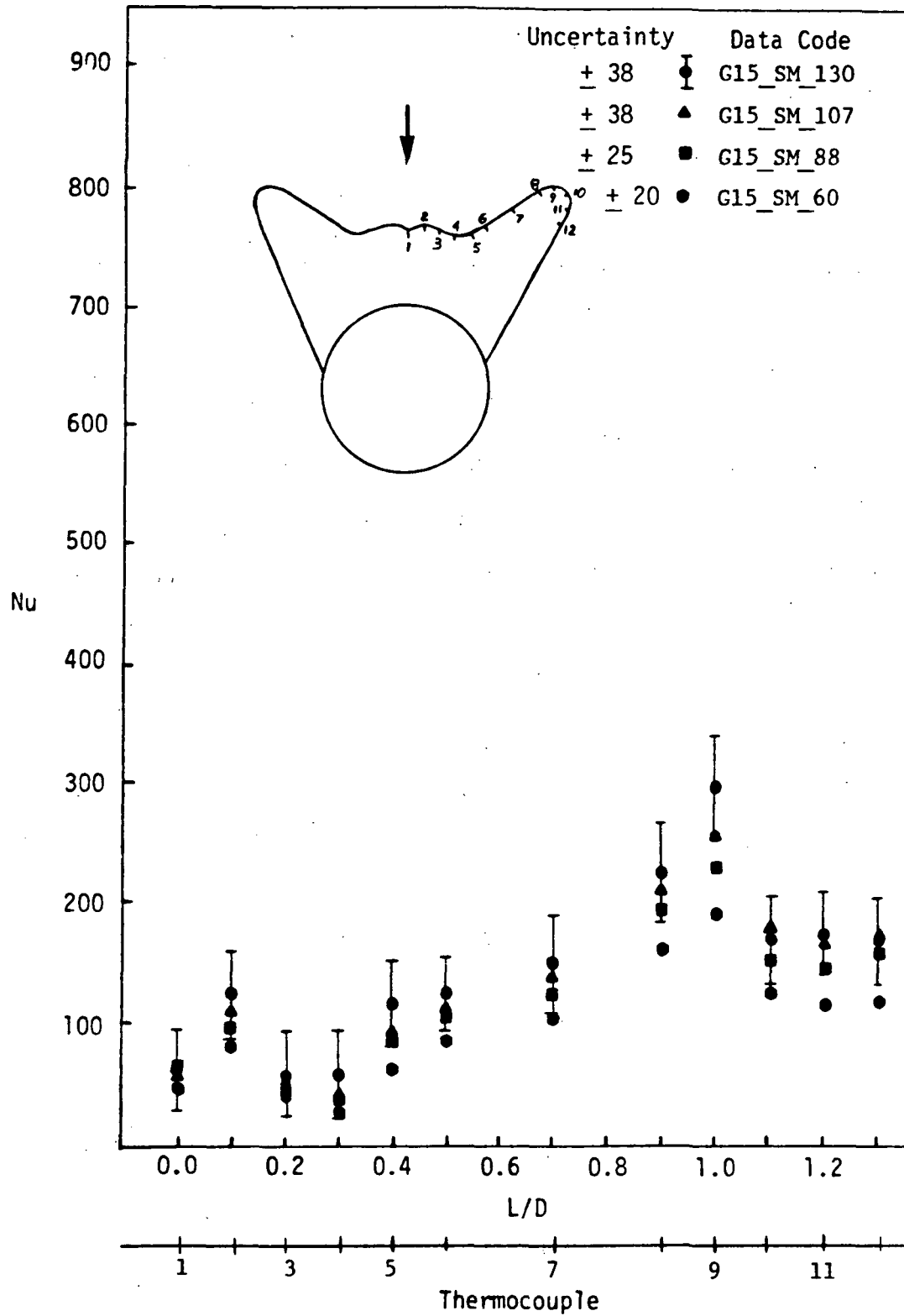


Figure 24. Nusselt Numbers for the Smooth 15-Minute Glaze Ice Shape.

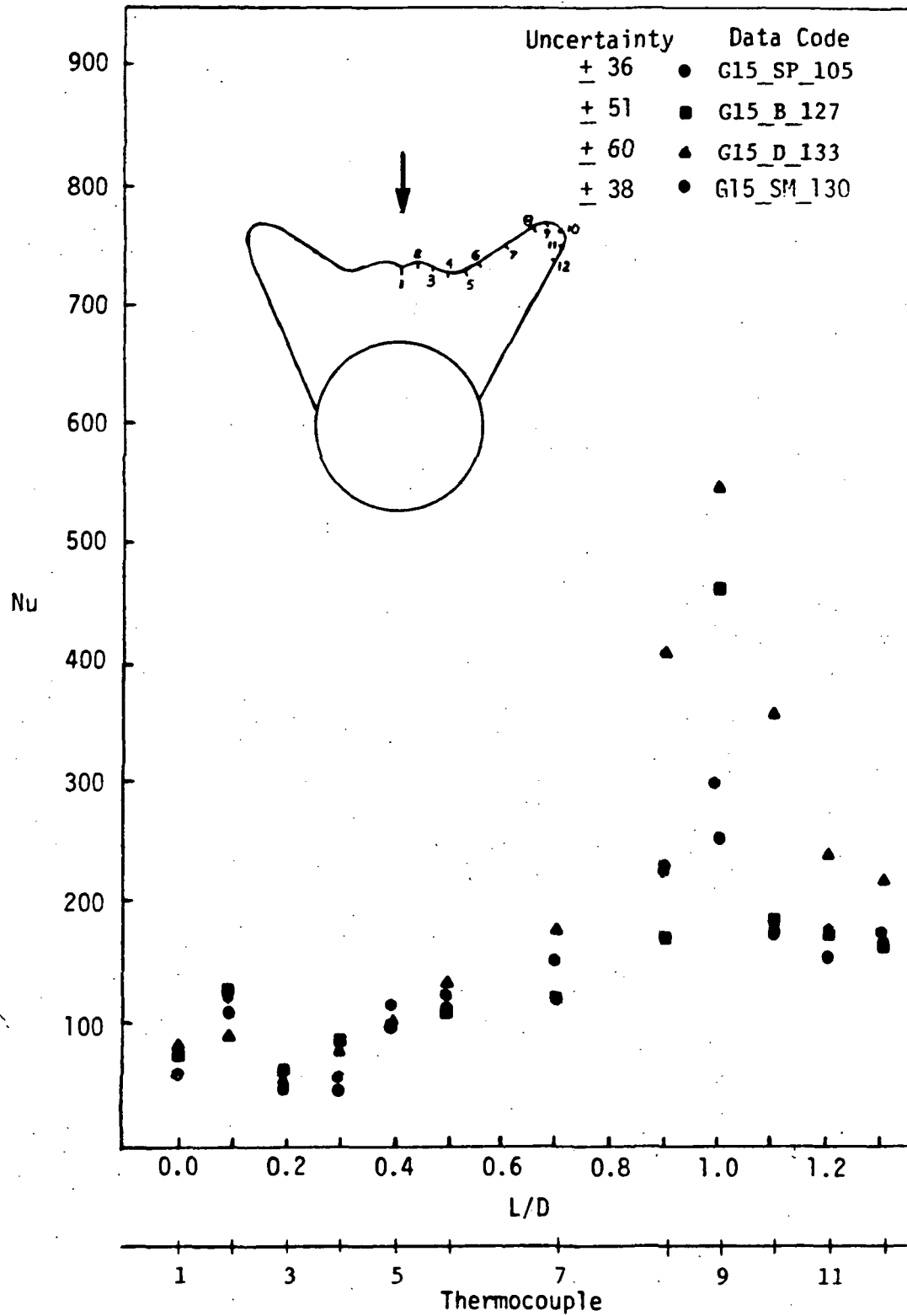


Figure 25. Nusselt Numbers for the Rough 15-Minute Glaze Ice Shape.

## APPENDIX A

### INITIAL TEMPERATURE-DISTRIBUTION EFFECTS

Non-uniform initial temperature distribution of the model skin was thought to be adversely affecting the data because of possible conduction errors. To investigate this possibility Figure 26 was prepared from data for the 15-minute rime ice shape. The figure gives the Nu obtained for tests in which the initial skin temperatures had ranges of variation of 42°F, 17°F, and 12°F. The improvements toward uniform initial temperature distribution, from 42°F to 17°F to 12°F, were obtained by successive modifications of the heating system.

A typical initial temperature distribution had a maximum temperature near the stagnation point of the model. From there the temperature dropped smoothly to a minimum at the point of contact between the skin and the wooden support.

From Figure 26 it was seen that for the conditions tested the non-uniformity of the initial temperature distribution had little affect on the Nu. The only significant effect of the non-uniformity appeared to be at the stagnation point. It was believed that this was a result not of the non-uniformity of the initial temperature but of the time variation of the Nu. For reasons not relevant to this discussion it was necessary to use data from a relatively long time after injection (approximately 1.4 sec) to calculate Nu for the 42°F range case. (The time variation of Nu was discussed in the Data Reduction section and the variation of Nu with time for the 15-minute rime ice shape was shown in Figure 8.) In this investigation it was observed that for early scans, the Nu distribution was similar to that for the 17°F and 12°F range cases (data for these was from early scans) and for later scans the Nu distribution was similar to that for the 42°F range case (for which the data was from later scans). It was thus concluded that the difference in

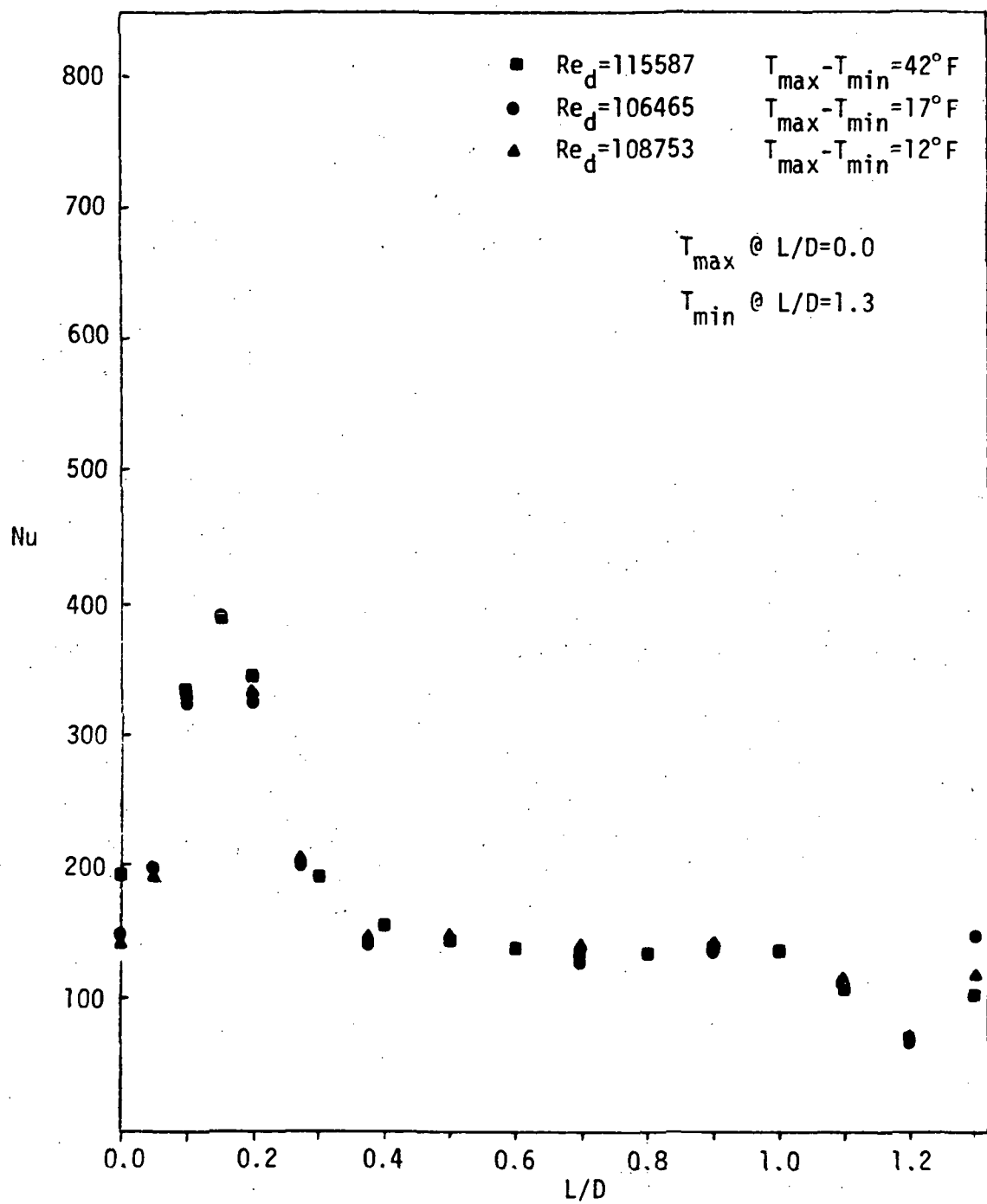


Figure 26. Initial Temperature Distribution Effects on Nusselt Numbers.  
 Data for the 15-minute rime ice shape.



Nu at the stagnation point was due to time variation of Nu rather than non-uniformity of the initial temperatures.

It was concluded that, based on this investigation, the non-uniformity of the initial skin temperature distributions discussed above had little affect on the resulting Nu. Nevertheless, to minimize the possibility of unforeseen problems, it was preferable to keep the range of variation of the initial temperatures to about 15°F or less. By modification of the heating arrangement this goal was achieved in all but a few cases. For those few cases the range was kept below 20°F.

# APPENDIX B

## COMPUTER PROGRAM FOR DATA ACQUISITION AND REDUCTION

```

10      !
20      ! BUFFDAT5
30      ! THIS PROGRAM WILL TAKE UP TO 60 VOLTMEETER
40      ! READINGS, STORE THEM IN COMPUTER MEMORY.
50      ! AND REPEAT THE PROCESS UP TO 20 TIMES.
60      PRINT "BEFORE USING THIS PROGRAM,CONNECT VM COMPLETE TO EXT INC."
70      CLEAR 709
80      INTEGER K,L,I,N,M,F,H      !THESE ARE COUNTERS
90      DIM AS$(20),Jf(20),Tl(20),A(20,60),T(37),V(37),Lntem(20,1000),Time(20,
100     60)
110     !AS=READINGS IN STRING FORMAT,A=READINGS
120     !IN NUMERIC FORMAT,Tf=TIME AT THE FIRST
130     !READING OF "Rdngs",Tl=TIME AT THE LAST
140     !READING OF "Rdngs".
150     Times=1      !Times *Rdngs =THE NUBER OF READINGS TAKEN
160     Chnls=12      !Chnls IS THE NUMBER OF CHANNELS
170     Rdngs=Chnls*5      !Rdngs IS THE NUMBER OF READINGS
180     Tl=TIMEDATE
190     K=0
200     ENABLE INTR 7:2      !K IS THE TIMES COUNTER
210     ON INTR 7.15 GOTO Interrupt      !ENABLE THE INTERRUPT BRANCH
220     !THIS TELLS THE COMPUTER WHAT TO DO
230     BS=VAL$(Chnls-1)      !WHEN IT GETS AN INTERRUPT SIGNAL
240     CS=VAL$(Rdngs)
250     OUTPUT 709:"AF00AL"&BS&"AC00AE1VT4VR1VA0VS!"
260     !THIS SETS UP THE 3497 UNIT
270     !AF00:THE FIRST CHANNEL IS 00
280     !ALYY:THE LAST CHANNEL IS YY
290     !AC00:CHANNEL 00 IS INITIALLY CLOSED
300     !AE1:USE THE EXTERNAL INCREMENT PORT
310     !VT4:SET VOLTMEETER TRIGGER TO HOLD

```

```

300 !VR1:SET VOLTMETER RANGE TO .1V
310 !VA0:TURN OFF THE AUTOZERO
320 !VS1:STORE READINGS IN THE BUFFER
330 OUTPUT 709;"SE1VN"&C$&"VT3"
340 !THIS TELLS THE 3497 TO EXECUTE THE COMANDS PREVIOUSLY SETUP
350 !SE1:SEND AN INTERRUPT WHEN THE DATA IS READY
360 !VNZZ:TAKE ZZ READINGS.ZZ=Rdngs
370 !VT3:TRIGGER THE VOLTMETER
380 Tf(K+1)=TIMEDATE !RECORD THE TIME OF THE FIRST READING OF Rdngs.
390 K=K+1 !INCREMENT THE TIMES COUNTER.
400 GOTO 400 !IDLE LOOP. WAIT FOR INTERRUPT.
410 !Interrupt IS THE SERVICE ROUTINE
420 Tl(K)=TIMEDATE !RECORD THE TIME OF THE LAST READING.
430 Serpoll=SPOLL(709) !POLL THEBUSS.CLEAR THE INTERRUPT.
440 OUTPUT 709;"VT4AE0VS"
450 !THIS SETS UP THE 3497 FOR SENDING THE READINGS TO THE
460 !COMPUTER
470 !VT4:SET VOLTMETER TRIGGER TO HOLD
480 !AE0:USE THE EXTERNAL INCREMENT PORT
490 !VS:MAKE DATA FROM THE BUFFER AVAILABLE
500 ENTER 709:AS(K)
510 !THE COMPUTER READS THE DATA IN THE BUFFER INTO AS
520 REM WAIT .65
530 IF K=Times THEN GOTO 570 !CHECK FOR TIMES REPEATED
540 ENABLE INTR 7:2 !REENABLE THE INTERRUPT BRANCH
550 GOTO 230 !TAKE Rdngs MORE READINGS
560 RETURN
570 GOTO 1360
580 !THE FOLLOWING CONVERTS THE STRING DATA TO NUMERIC DATA
590 P=0 ! P IS USED AS A SUBSCRIPT IN Lntem TO AID IN GRAPHING
600 ! L DESIGNATES WHICH BATCH OF READINGS
610 FOR L=1 TO Times
620 PRINT " CHANNEL TEMP LNTem Ht(B/H/TF) Nu"
630 FOR J=1 TO Rdngs
640 ! N IS A COUNTER,J IS THE READING WITHIN TIME L

```

```

650 N=((J-1)*12)+1
660 ! VOLTAGES ARE CONVERTED FROM STRING TO NUMERIC AND THE
670 ! REFERENCE VOLTAGE IS SUBTRACTED
680 A(L,J)=VAL(A$(L)[N:11])-VAL(A$(L)[(Chnls-1)*12)+1:11]
690 ! VOLTAGE A(L,J) IS CONVERTED TO A TEMPERATURE BY Tempr
700 V1=A(L,J)*1000
710 GOSUB Tempr
720 A(L,J)=Temp
730 NEXT J
740
750 ! M=CHANNEL, J IS THE READING WITHIN TIME L
760 ! Tsum IS USED IN THE CALCULATION OF Tfilm.
770 Cnt=0
780 M=0
790 Tsum=0
800 FOR J=1 TO Rdngs
810 ! THE TIME AT THE READING IS CALCULATED.
820 Time(L,J)=Tf(L)-Tf(1)+(T1(L)-Tf(L))/Rdngs*(J-1)
830 P=Time(L,J)*20
840 M=M+1
850 IF J>1.1 THEN GOTO 930
860 ! Tfilm IS CALCULATED.
870 Tr=A(L,Chnls-1)
880 FOR In=J TO J+Chnls-3
890 Tsum=Tsum+A(L,In)
900 NEXT In
910 Tavg=Tsum/(Chnls-2)
920 Tfilm=(Tavg+Tr)/2
930 PRINT USING "20X.AAAAAAAAAA.DDD.D,2X";"Tfilm IS".Tfilm
940 IF M<Chnls+1 THEN 1080
950 ! Tfilm IS CALCULATED FOR J>Chnls.
960 Tsum=0
970 PRINT " "
980 FOR In=J TO J+Chnls-3
990 Tsum=Tsum+A(L,In)
1000 NEXT In

```

```

1000 Cnt=Cnt+1
1010 Tr=A(L,Chnls-1+Cnt*Chnls)
1020 Tavg=Tsum/(Chnls-2)
1030 Tfilm=(Tavg+Tr)/2
1040 PRINT USING "20X.AAAAAAAA.DDD.D,2X":"Tfilm IS",Tfilm
1050 M=M-Chnls
1060
1070 GOTO 930
1080
1090 ! THE Nu IS CALCULATED IN THE FOLLOWING LINES
1100 IF M=Chnls-1 THEN 1610
1110 IF M=Chnls THEN 1610
1120 ! Lntem IS A PLOTTED PARAMETER
1130 Lntem(M,P)=(LOG(ABS((A(1,M)-A(L,Chnls-1)))/(A(L,J)-A(L,Chnls-1))))*100
1140 IF JK=Chnls THEN 1190
1150 ! Delt IS THE TIME BETWEEN THE PRESENT READING OF THIS
1160 ! CHANNEL AND THE PREVIOUS READING OF THIS CHANNEL
1170 Delt=Time(L,J)-Time(L,J-Chnls)
1180 ! DIntem IS USED IN THE CALCULATION OF Ht
1190 DIntem=(LOG(ABS((A(L,J-Chnls)-A(L,Chnls-1)))/(A(L,J)-A(L,Chnls-1))))*3
1200 600/Delt
1210 GOTO 1230
1220 IF L=1 THEN 1300
1230 Delt=Time(L,J)-Time(L-1,J+Rdngs-Chnls)
1240 DIntem=(LOG(ABS((A(L-1,J+Rdngs-Chnls)-A(L,Chnls-1)))/(A(L,J)-A(L,Chnls-1
1250 )))))*3600/Delt
1260 ! THE THERMAL CONDUCTIVITY OF THE AIR AT THE Tfilm
1270 Kt=(Tfilm-100)*.00002+.0154
1280 ! Ht IS THE HEAT TRANSFER COEFFICIENT IN BTU/Hr-SqFt-F
1290 Ht=.115*494*.015/12*DIntem
1300 ! Nu IS THE NUSSELT NUMBER CALCULATED USING A CHARACTERISTIC
1310 ! LENGTH OF 2.5 INCHES
1320 Nu=Ht*2.5/(Kt*12)
1330 GOTO 1310
1340 Ht=0
1350 PRINT USING "DDDD.DDD.2X":M,Time(L,J),A(L,J),Lntem(M,P),Ht,Nu
1360 NEXT J

```

```

1330 NEXT L
1340 GOTO 1640
1350
1360      !THIS IS DATA FOR Tempr
1370 DATA -30,-20,-10,0,10,20,30,40,50,60,70,80,90,100,110,120,130,140,150,160
1380 DATA 170,180,190,200,210,220,230,240,250,260,270,280,290,300,310,320,330
1390 FOR I=1 TO 37
1400 READ T(I)
1410 NEXT I
1420 DATA -1.279,-1.081,-.879,-.674,-.467,-.256,-.043,.173,.391,.611,.834,1.060
1430 DATA 1.288,1.518,1.752,1.988,2.226,2.467,2.711,2.958,3.206,3.458,3.711
1440 DATA 3.967,4.225,4.486,4.749,5.014,5.281,5.55,5.821,6.094,6.369,6.647
1450 DATA 6.926,7.207,7.490
1460 FOR I=1 TO 37
1470 READ V(I)
1480 NEXT I
1490 GOTO 580
1500 GOTO 1640
1510 Tempr: !THIS CONVERTS VOLTAGES TO TEMPERATURES BY LINEAR INTERPOLATION
1520 I=1
1530 IF V(I)<V1 THEN 1540
1540 GOTO 1570
1550 I=I+1
1560 IF I>37.1 THEN 1610
1570 GOTO 1520
1580 Temp=T(I-1)+(T(I)-T(I-1))*(V1-V(I-1))/(V(I)-V(I-1))
1590 GOTO 1590
1600 RETURN
1610 GOTO 1640
1620 Lntem(M,P)=99.999
1630 Ht=0
1640 GOTO 1310
1650 GCLEAR
1660 GINIT
1670 GRAPHICS ON
      AXES 10,10

```

```

1680      !HERE Lntem IS PLOTTED AGAINST TIME P
1690      !N AND M ARE USED AS DUMMY VARIABLES
1700      FOR N=1 TO Chnls-2
1710      CSIZE 4
1720      LINE TYPE 1
1730      MOVE 0:10
1740      LORG 5
1750      FOR M=1 TO P
1760      IF Lntem(N,M)=0 THEN 1800
1770      IF Lntem(N,M)<90 THEN 1790
1780      LABEL N
1790      DRAW M,(Lntem(N,M))+10
1800      NEXT M
1810      LABEL N
1820      NEXT N
1830      END

```

## APPENDIX C

### DATA REDUCTION

The equations used for data reduction are (the symbols are as defined for equation (1) in Chapter II)

$$h = \frac{\rho b c}{t_i - t_{i-1}} \ln \left[ \frac{T_{i-1} - T_{ri}}{T_i - T_{ri}} \right]$$

$$Nu = \frac{hd}{K}$$

where

$K$  = The thermal conductivity of air at  $T_{film}$

$d$  = The diameter of the cylinder (2.5 inches in all cases)

$$Re = \frac{U_{\infty} d}{\nu}$$

where

$U_{\infty}$  = free stream air speed

$\nu$  = kinematic viscosity for air at  $T_{film}$

$T_{film}$  was calculated by averaging the skin temperature and then averaging that temperature with the free stream temperature. The heat transfer coefficient is not very sensitive to changes in  $T_{film}$  for a cylinder[14]. Rearranging Frossling's equation for heat transfer at the stagnation point of a cylinder demonstrates this.

$$Nu = 0.9449 \sqrt{Re}$$

or

$$h = 0.9449 \frac{\sqrt{ud}}{d} \frac{K}{\sqrt{\nu}}$$



The temperature dependent term is  $K/\sqrt{v}$  which is not sensitive to temperature changes.

T(° F)	K(Btu/hr-ft-F)	$v(\text{ft}^2/\text{sec})$	$K/\sqrt{v}$
100	0.0154	$0.18 \times 10^{-3}$	1.148
150	0.0164	$0.21 \times 10^{-3}$	1.132
175	0.0169	$0.224 \times 10^{-3}$	1.129
200	0.0174	$0.239 \times 10^{-3}$	1.126

At one time during testing it was discovered that there was an error in the data reduction so that  $T_{\text{film}}$  was being calculated approximately 6% too high. Some of the data were re-reduced by hand to evaluate the effect the error had on final results. The difference in Nu numbers calculated using the high value of  $T_{\text{film}}$  and the correct value of  $T_{\text{film}}$  was less than 1%, which was negligible. Furthermore, since the Re was calculated using the same  $T_{\text{film}}$  as the Nu the error would tend to cancel when the Nu is considered with respect to the Re.

## APPENDIX D

### INITIAL PROBLEMS

A number of problems were encountered during initial testing and it may be of benefit to later experimenters to learn of these problems and thus avoid them.

The configuration for the first tests was as follows; the wooden support structure of the model was in direct contact with the skin except in the immediate vicinity of the thermocouples where there was a small air gap. Spot welding of the thermocouples had left indentations on the external surface of the skin at each thermocouple junction, and infrared heating elements were used to heat the skin. Results from the first test run were compared to the experimental results of Giedt [16]. Qualitatively, the results were in very good agreement with Giedt's. They followed the circumferential variation quite well. But they were all considerably lower than Giedt's results, especially at the higher Reynolds numbers. The results showed very little indication of any heat transfer effects other than convection (plots of the data were linear).

After concluding that the wooden model was affecting the apparent  $C_p$  of the skin, the model was modified so that there was a larger air space between the skin and the wood. Tests were rerun with all other conditions unmodified. The results improved slightly. Again there was little indication of conduction effects.

It had been noted in tests that there were circumferential temperature gradients as high as  $30^{\circ}\text{F}/\text{inch}$ , but since plots of the data were linear it was assumed that the conduction effects were negligible. It was then decided that despite the evidence of the plots the conduction effects were not negligible. The equipment was modified by replacing the radiant heating system with a conduction heating system. (The model was heated by the surrounding air which was in turn

heated by resistance heating elements.) With this system the initial skin temperature distribution could be held to gradients below  $4^{\circ}\text{F}/\text{inch}$ . Also, a data reduction procedure in which only data corresponding to relatively uniform skin temperature was adopted. Tests were rerun with this modification and again the results improved with respect to Giedt's results. The results were then compared to the Frossling equation, equation (10), and found to be in better agreement. An investigation into the discrepancy between Frossling's equation and Giedt's results revealed that Giedt's experiments had apparently been run in very turbulent flow although no turbulence level was stated. All subsequent comparisons were then made with respect to the Frossling equation.

Further refinement included rewelding the thermocouples so that the skin surface was not affected. With this modification the results discussed in the Test Results section were obtained.

**APPENDIX E**  
**TABLES OF NUSSELT NUMBERS**

The explanation for the Data Code appears in Chapter III on page 17. The location of the thermocouples on the Circular Cylinder is given in Figure 9 on page 40.

**Table 5. Nusselt Numbers for the Circular Cylinder with a Smooth Surface**

Data Code	Thermocouple									
	1	2	3	4	5	6	7	8	9	10
CC_SM_128	336	352	328	300	288	269	217	152	197	197
CC_SM_97	311	319	303	283	268	249	205	164	241	311
CC_SM_65	242	245	236	220	201	204	161	104	113	123

**Table 6. Nusselt Numbers for the Circular Cylinder with Roughness "B"**

Data Code	Thermocouple									
	1	2	3	4	5	6	7	8	9	10
CC_B_163	364	330	293	511	805	818	728	584	482	421
CC_B_128	293	273	231	360	679	684	605	480	392	281
CC_B_98	284	254	206	244	508	564	542	403	326	259
CC_B_65	202	191	165	138	250	373	403	351	275	208

**Table 7. Nusselt Numbers for the Circular Cylinder with Roughness "D"**

Data Code	Thermocouple									
	1	2	3	4	5	6	7	8	9	10
CC_D_128	306	337	398	493	564	587	—	435	401	418
CC_D_90	236	276	284	347	405	413	422	254	209	180
CC_D_63	195	227	299	265	301	312	—	176	176	145

(An explanation for the Data Code is on page 17)

The locations of the thermocouples for the 15-Minute rime shape are given in Figure 14 on page 45.

Table 8. Nusselt Numbers for the 15-Minute Rime Shape with a Smooth Surface

Data Code	Thermocouple												
	1	2	3	4	5	6	7	8	9	10	11	12	13
R15_SM_134	141	205	360	435	364	205	145	161	157	161	144	96	118
R15_SM_112	118	185	334	408	329	188	130	144	140	144	132	101	62
R15_SM_89	113	167	294	353	297	173	120	127	127	129	120	94	51
R15_SM-61	96	140	245	295	250	151	102	105	105	104	90	53	53

Table 9. Nusselt Numbers for the 15-Minute Rime Shape with a Sandpaper Strip Between Thermocouples 6 and 7

Data Code	Thermocouple												
	1	2	3	4	5	6	7	8	9	10	11	12	13
R15_SP_134	162	220	365	427	334	—	—	547	382	331	273	223	158

(An explanation for the Data Code is on page 17)

Table 10. Nusselt Numbers for the 15-Minute Rime Shape with Roughness "B"

Data Code	Thermocouple												
	1	2	3	4	5	6	7	8	9	10	11	12	13
R15_B_136	127	168	252	324	279	334	532	505	486	498	425	423	319
R15_B_117	123	164	246	312	269	301	511	477	433	461	398	393	318
R15_B_88	110	143	217	272	223	204	411	413	379	387	342	324	266
R15_B_62	72	114	169	229	168	100	343	317	279	288	245	235	197

Table 11. Nusselt Numbers for the 15-Minute Rime Shape with Roughness "D"

Data Code	Thermocouple												
	1	2	3	4	5	6	7	8	9	10	11	12	13
R15_D_140	158	199	340	467	607	589	463	481	412	381	396	327	211
R15_D_118	145	180	312	417	527	514	404	423	363	332	339	275	187
R15_D_89	106	145	244	331	417	392	270	297	265	239	252	195	141
R15_D_64	95	121	206	258	294	289	208	245	220	186	193	156	120

The locations of the thermocouples for the 2-minute glaze shape are given in Figure 17 on page 49.

Table 12. Nusselt Numbers for the 2-Minute Glaze Shape with a Smooth Surface

Data Code	Thermocouple									
	1	2	3	4	5	6	7	8	9	10
G2_SM_134	247	248	287	287	286	244	213	183	201	148
G2_SM_113	234	236	269	256	245	228	197	163	163	131
G2_SM_88	197	200	233	221	211	202	173	144	130	102
G2_SM_61	169	170	196	185	176	166	141	109	87	84

Table 13. Nusselt Numbers for the 3-Minute Glaze Shape with a Sandpaper strip Between Thermocouples 3 and 4.

Data Code	Thermocouple									
	1	2	3	4	5	6	7	8	9	10
G2_SP_134	236	238	—	—	403	304	254	192	227	166
G2_SP_112	227	219	—	—	317	247	210	162	183	129
G2_SP_87	200	196	—	—	243	194	170	141	115	104
G2_SP_60	172	170	—	—	193	167	146	114	107	78

(An explanation for the Data Code is on page 17)



Table 14. Nusselt Numbers for the 2-Minute Glaze Shape with Roughness "B"

Data Code	Thermocouple									
	1	2	3	4	5	6	7	8	9	10
G2_B_132	209	224	280	565	596	628	575	259	236	148
G2_B_113	188	191	251	502	543	555	515	237	218	139
G2_B_88	173	165	207	330	405	430	407	180	166	110
G2_B_60	138	130	163	97	197	291	314	144	134	84

Table 15. Nusselt Numbers for the 2-Minute Glaze Shape with Roughness "D"

Data Code	Thermocouple									
	1	2	3	4	5	6	7	8	9	10
G2_D_138	227	234	337	569	565	536	560	286	172	163
G2_D_112	181	202	290	472	484	448	472	230	145	135
G2_D_90	156	172	222	387	410	385	399	180	110	110
G2_D_61	150	150	180	261	288	288	301	140	82	70

(An explanation for the Data Code is on page 17)

The locations of the thermocouples are for the 5 minute glaze shape are given in Figure 20 on page 53.

Table 16. Nusselt Numbers for the 5-Minute Glaze Shape with a Smooth Surface

Data Code	Thermocouple									
	1	2	3	4	5	6	7	8	9	10
G5_SM_134	100	240	259	55	82	291	343	202	209	260
G5_SM_113	76	204	218	49	72	266	310	185	176	235
G5_SM_90	90	180	186	53	71	222	271	164	146	177
G5_SM_64	73	156	176	64	64	181	228	144	135	170

Table 17. Nusselt Numbers for the 5-Minute Glaze Shape with a Sandpaper Strip Between Thermocouples 3 and 4.

Data Code	Thermocouple									
	1	2	3	4	5	6	7	8	9	10
G5_SP_135	74	162	—	—	265	468	661	227	189	207
G5_SP_113	76	173	—	—	243	407	583	159	166	189
G5_SP_88	53	128	—	—	129	327	407	154	124	159
G5_SP_59	42	114	—	—	46	199	186	126	107	134

(An explanation for the Data Code is on page 17)

**Table 18. Nusselt Numbers for the 5-Minute Glaze Shape with Roughness "B"**

Data Code	Thermocouple									
	1	2	3	4	5	6	7	8	9	10
G5_B_135	106	225	177	72	249	506	457	210	252	292
G5_B_113	69	210	163	55	194	443	411	165	218	255
G5_B_86	76	180	147	36	103	358	342	153	183	210
G5_B_61	60	149	119	29	62	261	273	146	134	191

**Table 19. Nusselt Numbers for the 5-Minute Glaze Shape with Roughness "D"**

Data Code	Thermocouple									
	1	2	3	4	5	6	7	8	9	10
G5_D_135	91	219	237	218	323	360	616	429	266	286
G5_D_114	73	191	192	138	251	317	547	345	235	250
G5_D_89	81	169	173	118	229	316	461	293	200	199
G5_D_62	59	127	131	70	133	218	349	209	162	171

(An explanation for the Data Code is on page 17)

The locations of the thermocouples for the 15 minute glaze shape are given in Figure 23 on page 57.

Table 20. Nusselt Numbers for the 15-Minute Glaze Shape with a Smooth Surface

Data Code	Thermocouple											
	1	2	3	4	5	6	7	8	9	10	11	12
GI5_SM_130	60	123	53	55	114	124	147	223	294	169	172	167
GI5_SM_107	57	109	52	38	91	111	135	209	252	176	161	170
GI5_SM_88	62	97	46	37	84	104	124	192	229	149	143	156
GI5_SM_60	44	81	39	25	60	83	103	159	189	124	115	117

Table 21. Nusselt Numbers for the 15-Minute Glaze Shape with a Sandpaper Strip Between Thermocouples 7 and 8.

Data Code	Thermocouples											
	1	2	3	4	5	6	7	8	9	10	11	12
GI5_SP_105	57	108	46	42	95	111	119	228	254	173	152	166
GI5_SP_86	46	101	45	36	83	98	111	195	235	155	149	143
GI5_SP_62	35	84	38	21	62	83	93	169	195	122	99	110

(An explanation for the Data Code is on page 17)

Table 22. Nusselt Numbers for the 15-Minute Glaze Shape with Roughness "B"

Data Code	Thermocouple											
	1	2	3	4	5	6	7	8	9	10	11	12
Gl5_B_127	72	125	59	83	96	109	121	169	461	184	170	159
Gl5_B_108	50	93	37	50	83	99	108	156	319	189	172	166
Gl5_B_88	42	79	36	33	61	63	90	143	192	166	153	134
Gl5_B_61	34	65	28	27	55	71	80	122	94	108	115	110

Table 23. Nusselt Numbers for the 15-Minute Glaze Shape with Roughness "D"

Data Code	Thermocouple											
	1	2	3	4	5	6	7	8	9	10	11	12
Gl5_D_133	80	87	52	74	103	131	175	406	545	354	237	218
Gl5_D_108	46	91	32	77	92	113	122	297	440	271	161	190
Gl5_D_89	58	51	36	57	84	90	129	280	395	239	183	158
Gl5_D_64	36	41	29	28	75	67	81	119	209	146	118	122

(An explanation for the Data Code is on page 17)

**APPENDIX F**  
**UNCERTAINTY ANALYSIS**

$$Nu = \frac{dh}{K} = \frac{d\rho bc}{K(t_i - t_{i-1})} \ln \frac{T_{i-1} - T_{ri}}{T_i - T_{ri}}$$

The uncertainty of the Nu can be written as[15]

$$\omega_{Nu} = \left[ (\omega_d \frac{\partial Nu}{\partial d})^2 + (\omega_\rho \frac{\partial Nu}{\partial \rho})^2 + \dots + (\omega_{T_{ri}} \frac{\partial Nu}{\partial T_{ri}})^2 \right]^{1/2} \quad (11)$$

Substituting the differentiated terms and dividing by Nu gives

$$\begin{aligned} \frac{\omega_{Nu}}{Nu} = & \left[ \left(\frac{\omega_d}{d}\right)^2 + \left(\frac{\omega_\rho}{\rho}\right)^2 + \left(\frac{\omega_b}{b}\right)^2 + \left(\frac{\omega_c}{c}\right)^2 + \left(\frac{\omega_K}{K}\right)^2 \right. \\ & + 2 \left(\frac{\omega_t}{\Delta t}\right)^2 + \left(\frac{\omega_{T_{i-1}}}{A(T_{i-1} - T_{ri})}\right)^2 + \left(\frac{\omega_{T_i}(T_{ri} - T_{i-1})}{A(T_i - T_{ri})^2}\right)^2 \\ & \left. + \left(\frac{\omega_{T_{ri}}(T_{i-1} - T_i)}{A(T_{i-1} - T_{ri})(T_i - T_{ri})}\right)^2 \right]^{1/2} \quad (12) \end{aligned}$$

where

$$\Delta t = (t_i - t_{i-1})$$

$$A = \ln \left[ \frac{T_{i-1} - T_{ri}}{T_i - T_{ri}} \right]$$

Estimates of the individual uncertainties are

$$d = 2.5 \pm 0.125 \text{ in.}$$

$$K = 0.017 \pm 2 \times 10^{-4} \text{ Btu/hr-ft-}^\circ\text{F}$$

$$\rho = 494 \pm 10 \text{ lbm/ft}^3$$

$$b = 0.015 \pm 2.25 \times 10^{-4} \text{ in.}$$

$$c = 0.115 \pm 0.007 \text{ Btu/lbm-}^\circ\text{F}$$

$$\Delta t = 0.285 \text{ sec uncertainty on } t = \pm 0.001 \text{ sec}$$

$$T_{ri} = 79 \pm 0.5 \text{ }^\circ\text{F}$$

$$T_{i-1} = 290 \pm 0.5 \text{ }^\circ\text{F}$$

$$T_i = 285^\circ \pm 0.5 \text{ }^\circ\text{F}$$

Using these values the uncertainty is

$$\frac{w_{Nu}}{Nu} = \pm 16\%$$

However, the uncertainty is sensitive to  $T_i$  and  $T_{i-1}$  and highly sensitive to the difference between them. As the difference becomes small the log term,  $A$ , goes to zero and the uncertainty increases dramatically. Small differences in  $T_i$  and  $T_{i-1}$  correspond to low  $Nu$ . It was found that if the uncertainties were expressed in units of  $Nu$  rather than as percentages the uncertainty bands had less variance.

The uncertainty for the  $Re$  is calculated in a similar fashion using the values

$$U_\infty = 100 \pm 1 \text{ mph}$$

$$\nu = 2.3 \times 10^{-4} \pm 0.05 \times 10^{-6} \text{ ft}^2/\text{sec}$$

$$\frac{w_{Re}}{Re} = \pm 6\%$$

## APPENDIX G

### COMPARISON TO NASA TESTS

When testing the 15 minute rime ice shape it was found that the results predicted a Nu approximately 50% below the Nu predicted by NASA in-house tests[13]. Investigation of the NASA data revealed that a transition was occurring in the flow at a Re number of 60,000 as indicated in Figure 27. The transition did not occur in tests for the present study. It is believed that the transition was not present due to differences in the model and the flow conditions.

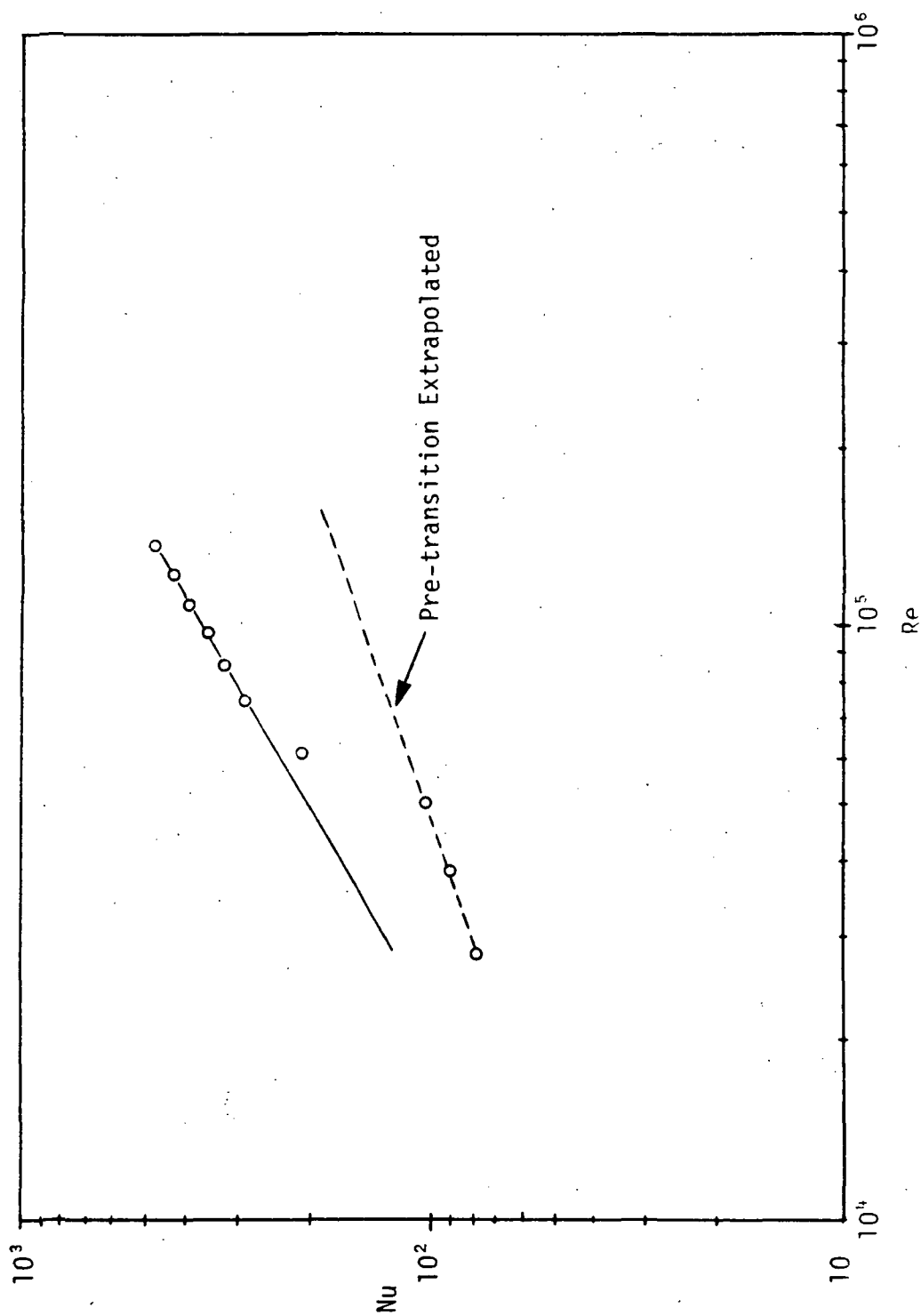
To investigate further, the NASA pre-transition data was extrapolated to a Re range comparable to the range used in this study. Figure 28 shows how the experimental results compare to the extrapolated NASA results. There is good agreement particularly in the region from  $L/D = 0.4$  to  $0.7$ . The differences apparent in the regions  $L/D = 0.05$  to  $0.4$  and  $0.8$  to  $1.1$  were likely due to differences between the NASA model and the UTK model. The curvature around the nose of the NASA model was much sharper than that of the UTK model, see Figure 15 and 29. A comparison of the approximate radii in this region is given below.

Model	r(in)	d(in)	r/d
NASA	0.11	2.0	0.055
UTK	0.25	2.5	0.1

r = Radius of curvature

d = Base cylinder diameter





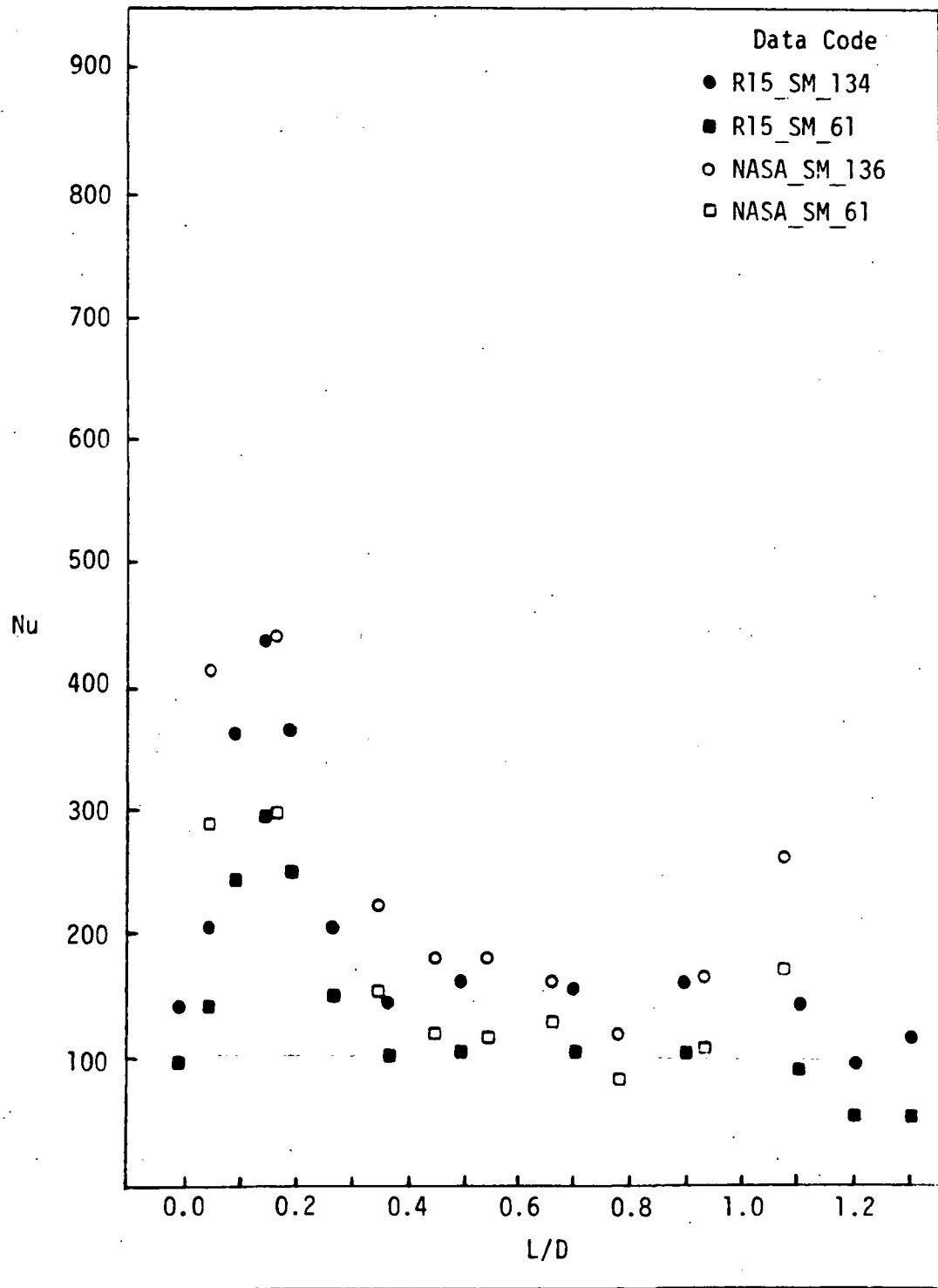


Figure 28. Nusselt Numbers for the Smooth 15-Minute Rime Ice Shape  
Extrapolated From NASA Pre-transition Data.

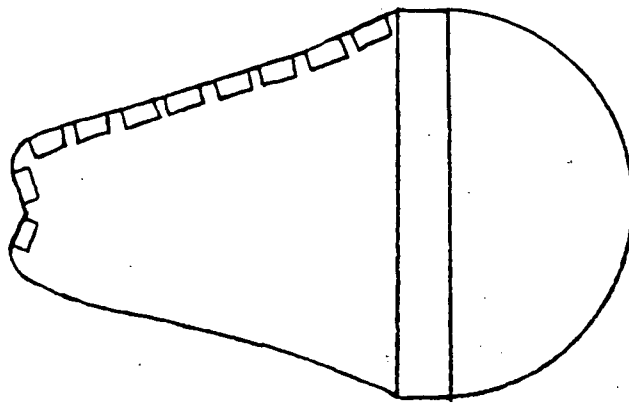


Figure 29. The NASA Model for the 15-Minute Rime Ice Shape.

The effective radius of curvature was nearly twice as sharp for the NASA model. The local velocity would be expected to be higher around the smaller radius and thus the heat transfer would be greater.

In the region  $L/D = 0.8$  to  $1.1$  the NASA model had a slightly concave curvature. On the UTK's model there was a slightly convex curvature in this region.

Several combinations of trip wires and sandpaper trips were tested on the model. Figure 30 shows that the trip wires on the model effectively brought the  $Nu$  up to the levels reported by NASA for the smooth surface and fully turbulent flow. Figure 31 shows the same trend when sandpaper trips were used. Figure 32 shows roughness "B" compared to the NASA data. Except near the nose of the model the data falls between the smooth and rough surface data.

Also, it is believed that with roughness "B" the trip wires not only induced, turbulence but thickened the boundary layer. The thermocouples were always situated in the "valleys" between the wires which may have been relatively stagnant regions. It would have been preferable to use an average of measurements for peaks and valleys but the thin-skin method precluded such measurements.

The conclusion based on extensive testing of the 15 minute rime ice shapes are:

1. The NASA tests had a transition that did not appear in this study which was speculated to be due to differences in the models and flow conditions,
2. The methods and results of this study are best suited to smooth surfaced models,
3. With proper duplication of the conditions of the NASA tests the NASA results could also be duplicated.

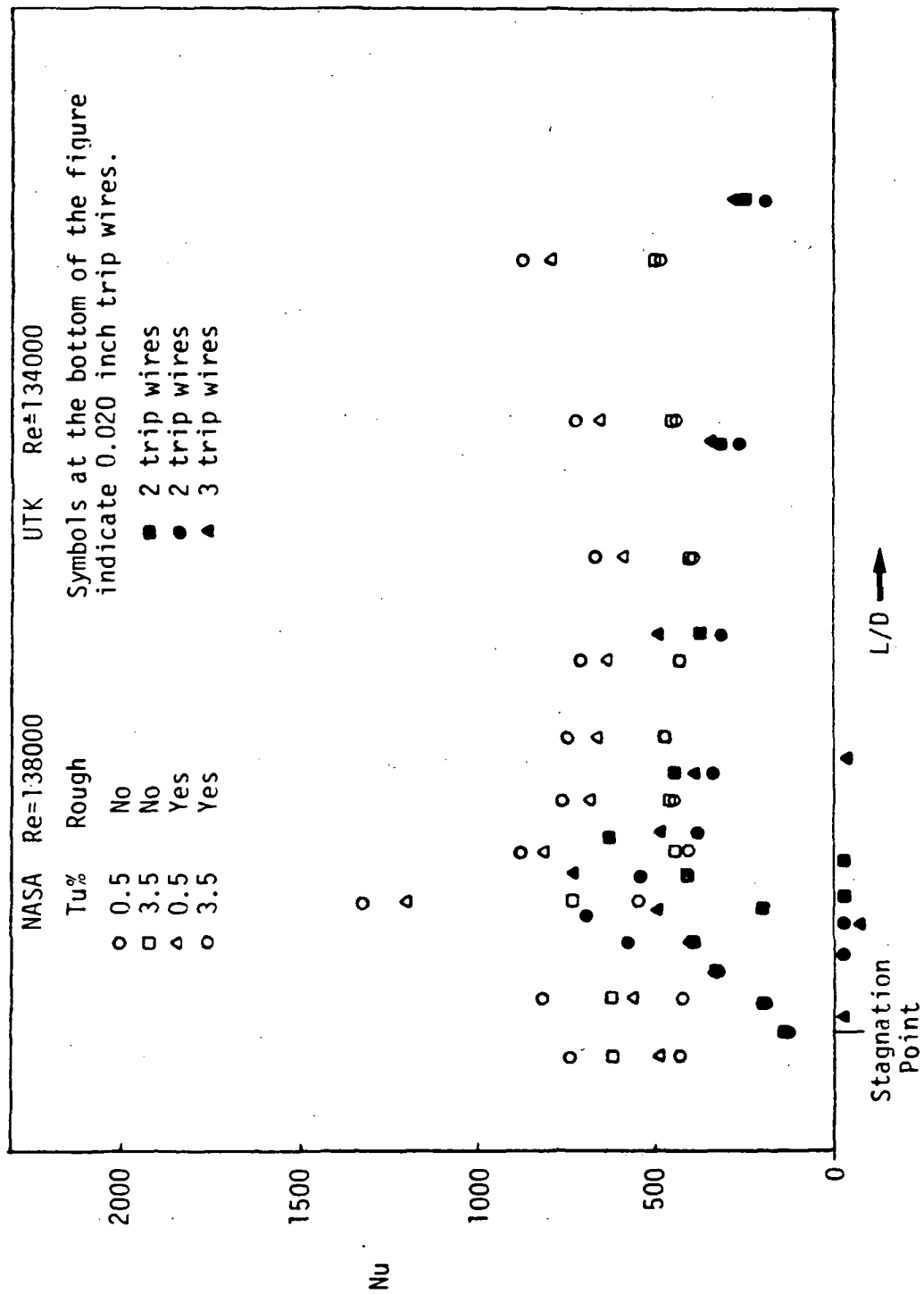


Figure 30. Nusselt Numbers From NASA Tests and UTK Tests With Trip Wires.

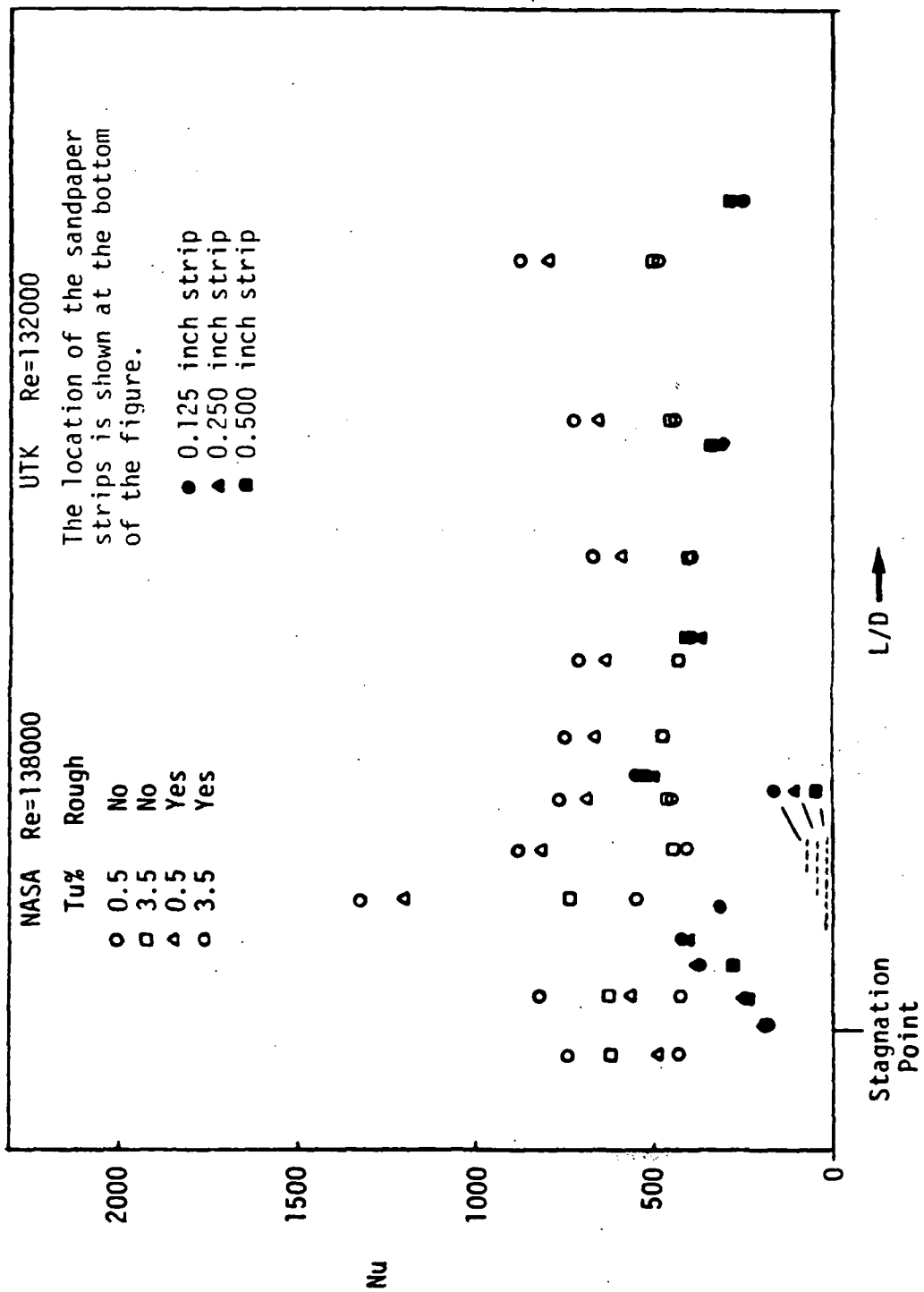


Figure 31. Nusselt Numbers From NASA Tests and UTK Tests With Sandpaper Strips.

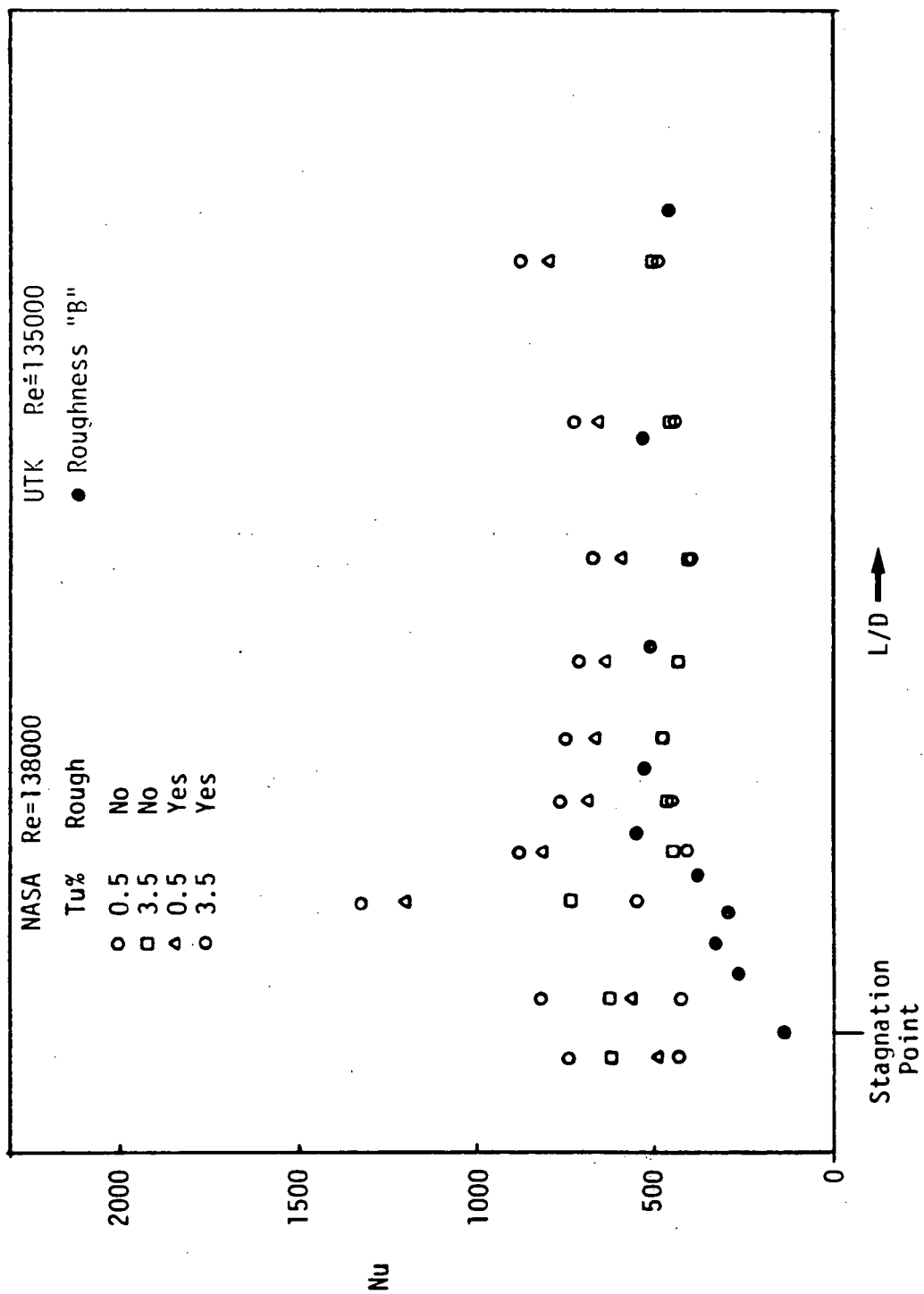


Figure 32. Nusselt Numbers From NASA Tests and UTK Tests With Roughness "B".

## APPENDIX H

### VALIDITY OF LUMPED SYSTEM ASSUMPTION

One assumption that the thin-skin method makes is that the outside skin temperature is the same as the inside skin temperature. To ensure that the assumption was valid the Biot number for the system was made much less than 1.

$$Bi = \frac{hb}{K}$$

For some conservative values the Bi is

$$Bi = 0.009$$

where

$$h = 80 \frac{\text{Btu}}{\text{hr-ft}^2-\text{°F}}$$

$$K = 11 \frac{\text{Btu}}{\text{hr-ft-°F}}$$

$$b = 0.015 \text{ in.}$$



1. Report No. <b>NASA CR-174680</b>		2. Government Accession No.		3. Recipient's Catalog No.	
4. Title and Subtitle <b>Measurement of Local Convective Heat Transfer Coefficients of Four Ice Accretion Shapes</b>				5. Report Date <b>May 1984</b>	
				6. Performing Organization Code	
7. Author(s) <b>Mark E. Smith, Rao V. Armilli, and Edward G. Keshock</b>				8. Performing Organization Report No. <b>None</b>	
				10. Work Unit No.	
9. Performing Organization Name and Address <b>The University of Tennessee Mechanical and Aerospace Engineering Dept. Knoxville, Tennessee 37996-2210</b>				11. Contract or Grant No. <b>NAG-3-83</b>	
				13. Type of Report and Period Covered <b>Contractor Report</b>	
12. Sponsoring Agency Name and Address <b>National Aeronautics and Space Administration Washington, D.C. 20546</b>				14. Sponsoring Agency Code <b>505-45-02</b>	
15. Supplementary Notes <b>Final report. Project Manager, Robert J Shaw, Propulsion Systems Division, NASA Lewis Research Center, Cleveland, Ohio 44135.</b>					
16. Abstract <b>In the analytical study of ice accretions that form on aerodynamic surfaces (airfoils, engine inlets, etc.) it is often necessary to be able to calculate convective heat transfer rates. In order to do this, local convective heat transfer coefficients for the ice accretion shapes must be known. In the past, coefficients obtained for circular cylinders were used as an approximation to the actual coefficients since no better information existed. The purpose of this experimental study was to provide local convective heat transfer coefficients for four shapes that represent ice accretions. The shapes were tested with smooth and rough surfaces. The experimental method chosen was the thin-skin heat rate technique. Using this method local Nusselt numbers were determined for the ice shapes. In general it was found that the convective heat transfer was higher in regions where the model's surfaces were convex and lower in regions where the model's surfaces were concave. The effect of roughness was to increase the heat transfer in the high heat transfer regions by approximately 100% while little change was apparent in the low heat transfer regions.</b>					
17. Key Words (Suggested by Author(s)) <b>Aircraft icing Ice accretion shapes Convective heat transfer coefficient Experimental measurements Thinskin heat rate technique</b>				18. Distribution Statement <b>Unclassified - unlimited STAR Category 02</b>	
19. Security Classif. (of this report) <b>Unclassified</b>		20. Security Classif. (of this page) <b>Unclassified</b>		21. No. of pages <b>94</b>	
				22. Price* <b>A05</b>	

National Aeronautics and  
Space Administration

Washington, D.C.  
20546

Official Business

Penalty for Private Use, \$300

SPECIAL FOURTH CLASS MAIL  
BOOK



Postage and Fees Paid  
National Aeronautics and  
Space Administration  
NASA-451

**NASA**

POSTMASTER:

If Undeliverable (Section 154  
Postal Manual) Do Not Return

---